NASA Technical Paper 1345

Analysis of Supersonic Stall Bending Flutter in Axial-Flow Compressor by Actuator Disk Theory

John J. Adamczyk

NOVEMBER 1978

NASA

NASA Technical Paper 1345

Analysis of Supersonic Stall Bending Flutter in Axial-Flow Compressor by Actuator Disk Theory

John J. Adamczyk
Lewis Research Center
Cleveland, Ohio

NASA
National Aeronautics
and Space Administration

Scientific and Technical Information Office

1978

SUMMARY

An analytical model was developed for predicting the onset of supersonic stall bending flutter in axial-flow compressors. The analysis is based on a modified two-dimensional, compressible, unsteady actuator disk theory. It is applied to a rotor blade row by considering a cascade of airfoils whose geometry and dynamic response coincide with those of a rotor blade element at 85 percent of the span height (measured from the hub). The rotor blades are assumed to be unshrouded (i.e., free standing) and to vibrate in their first flexural mode. The effects of shock waves and flow separation are included in the model through quasi-steady, empirical, rotor total-pressure-loss and deviation-angle correlations.

The actuator disk model predicts the unsteady aerodynamic force acting on the cascade blading as a function of the steady flow field entering the cascade and the geometry and dynamic response of the cascade. Calculations show that the present model predicts the existence of a bending flutter mode at supersonic inlet Mach numbers. This flutter mode is suppressed by increasing the reduced frequency of the system or by reducing the steady-state aerodynamic loading on the cascade. The validity of the model for predicting flutter is demonstrated by correlating the measured flutter boundaries of several high-speed fan stages with their predicted boundaries. This correlation uses a level of damping for the blade row (i.e., the log decrement of the rotor system) that is estimated from the experimental flutter data. The predicted flutter boundaries are in good agreement with the measured boundaries.

These results show that the model can be used to estimate the relative stability between operating points of a given rotor system. If, in addition, a measure of the mechanical damping of the rotor system is available, the model can also be used to estimate the absolute stability at an operating point.

INTRODUCTION

Flutter can result in costly (both in time and money) overruns in turbofan-engine development programs. Solving the problem of flutter (at the engine development stage) may well mean major engine redesign and retesting. For this reason, engine manufacturers and government agencies are currently supporting numerous research programs in an attempt to develop flutter prediction systems that can be used to design flutter-free engines. To date, these research programs have identified five regions (fig. 1) of the

compressor performance map where flutter is generally encountered.

Of the five regions shown in figure 1, the supersonic low-backpressure flutter region has been the most thoroughly investigated analytically (refs. 1 to 3). In general, these analyses have considered the flow field through a cascade of two-dimensional airfoils undergoing simple harmonic pitching or plunging. The gas stream was assumed to be an inviscid, nonconducting, perfect gas. Shock waves that originated in the flow field were assumed to be weak so that supersonic small-disturbance theory could be used. Although these assumptions appear to oversimplify the flow conditions encountered by a rotor at the onset of flutter, the flutter boundaries predicted by these analyses correlate well with experimental data.

A recent analysis (ref. 4) has attempted to apply the supersonic, linearized, small-disturbance theory to higher backpressure operating conditions (i.e., region IV of fig. 1) by including a finite-strength shock wave within the cascade passage. Results from this analysis show that the unsteady motion of the shock wave tends to induce bending flutter. The existence of this flutter mode is documented in reference 5.

The remaining operating region where supersonic flutter occurs (region V of fig. 1) lies close to the stall line of a stage. Analyses of this region have not appeared in the open literature. Literature on this subject (e.g., refs. 5 to 7) generally presents experimental data to document the extent of the flutter region. These data provide a very limited base from which an empirical correlation can be derived for predicting the onset of this flutter mode.

The objective of the present analysis is to develop a model for predicting the onset of supersonic stall flutter. The calculated flutter boundaries of four high-speed fan stages that have experienced this type of flutter are compared with their measured boundaries to validate the analysis.

BACKGROUND

Supersonic stall flutter is generally encountered by rotors that do not have part-span dampers or tip shrouds. Experimental data reveal that the flutter mode is generally the first flexural mode at a reduced frequency (based on tip relative velocity and tip semichord) of about 0.2. The vibratory pattern around the rotor tends to be very regular: All blades vibrate at the same frequency but are shifted in phase by a positive interblade phase angle of about 20° to 50° (ref. 7). This positive phase shift implies that the vibratory pattern is traveling around the wheel in the direction of rotation (i.e., a forward-traveling wave).

A further characteristic of fans operating in flow regions associated with stall flutter is shown by the steady-state pressure distribution in figure 2. This pressure distribution was produced from measurements taken across a rotor tip while the rotor was

compressor performance map where flutter is generally encountered.

Of the five regions shown in figure 1, the supersonic low-backpressure flutter region has been the most thoroughly investigated analytically (refs. 1 to 3). In general, these analyses have considered the flow field through a cascade of two-dimensional airfoils undergoing simple harmonic pitching or plunging. The gas stream was assumed to be an inviscid, nonconducting, perfect gas. Shock waves that originated in the flow field were assumed to be weak so that supersonic small-disturbance theory could be used. Although these assumptions appear to oversimplify the flow conditions encountered by a rotor at the onset of flutter, the flutter boundaries predicted by these analyses correlate well with experimental data.

A recent analysis (ref. 4) has attempted to apply the supersonic, linearized, small-disturbance theory to higher backpressure operating conditions (i.e., region IV of fig. 1) by including a finite-strength shock wave within the cascade passage. Results from this analysis show that the unsteady motion of the shock wave tends to induce bending flutter. The existence of this flutter mode is documented in reference 5.

The remaining operating region where supersonic flutter occurs (region V of fig. 1) lies close to the stall line of a stage. Analyses of this region have not appeared in the open literature. Literature on this subject (e.g., refs. 5 to 7) generally presents experimental data to document the extent of the flutter region. These data provide a very limited base from which an empirical correlation can be derived for predicting the onset of this flutter mode.

The objective of the present analysis is to develop a model for predicting the onset of supersonic stall flutter. The calculated flutter boundaries of four high-speed fan stages that have experienced this type of flutter are compared with their measured boundaries to validate the analysis.

BACKGROUND

Supersonic stall flutter is generally encountered by rotors that do not have part-span dampers or tip shrouds. Experimental data reveal that the flutter mode is generally the first flexural mode at a reduced frequency (based on tip relative velocity and tip semichord) of about 0.2. The vibratory pattern around the rotor tends to be very regular: All blades vibrate at the same frequency but are shifted in phase by a positive interblade phase angle of about 20° to 50° (ref. 7). This positive phase shift implies that the vibratory pattern is traveling around the wheel in the direction of rotation (i.e., a forward-traveling wave).

A further characteristic of fans operating in flow regions associated with stall flutter is shown by the steady-state pressure distribution in figure 2. This pressure distribution was produced from measurements taken across a rotor tip while the rotor was

operating near the flutter boundary. This figure clearly indicates a detached, leading-edge bow shock wave impinging on the suction surface of the adjacent blade. The large extent of the compression region at the base of the shock wave seems to suggest a separated flow region that would increase in size as the fan operating point moved toward the supersonic stall bending flutter boundary. This separated flow would be accompanied by a decrease in shock strength.

The present analysis develops a flutter model for the highly complicated flow field illustrated in figure 2 by using two-dimensional actuator disk theory. The effects of flow separation are included in the model through rotor-loss and deviation-angle correlations. For low-speed flows, actuator disk flutter models have been able to predict the onset of a single-degree-of-freedom bending flutter mode (e.g., refs. 8 and 9). The success of the models at low speeds suggests that a compressible actuator disk model might be capable of predicting the onset of bending flutter at supersonic speeds. This hypothesis has been confirmed by a number of calculations. These calculations, however, did require as input the interblade phase angle at the onset of flutter. So that this requirement could be avoided, the actuator disk model was modified to allow for moderate values of interblade phase angle. This modification results in a flutter model that can be developed into a flutter prediction system. The validity of this flutter prediction system is demonstrated by comparing the predicted flutter boundaries of four high-speed fan stages with their measured boundaries.

FORMULATION

The present analysis for stall bending flutter of an isolated rotor models the rotor as a two-dimensional cascade of airfoils. The cascade is defined by the blade-element geometry on a cylindrical surface at a distance R from the axis of rotation. The flow field in the cascade plane is assumed to be two dimensional, compressible, and time dependent. Viscous forces are considered only within the blade channel. The unsteady flow variables associated with the rotor vibratory motion are assumed to be smaller than their steady-state counterparts. These variables at an instant in time are required to be periodic around the wheel at a period equal to a fractional part of the circumferential distance $d = 2\pi R$.

The motion of the airfoils in the cascade plane is restricted to simple harmonic plunging and edgewise motion at a cyclic frequency ω (fig. 3). In addition the motion of each airfoil at an instant in time is assumed to be shifted from that of its neighbor by an interblade phase angle of $\sigma = 2\pi n/N$, where n is an integer and N is the number of blades in the rotor. In the present analysis the reduced-frequency parameter k_b and the interblade phase angle are assumed to be small. Reduced frequency $k_b = \omega b/\overline{q}_{-\infty}$,

where b is the semichord of an airfoil and $\overline{q}_{-\infty}$ is the magnitude of the relative inlet velocity in the cascade plane.)

Field Equations

The governing equations for the flow field upstream and downstream of the cascade are written with respect to the relative coordinate system. The variables in these equations are nondimensionalized by the parameter $\overline{q}_{-\infty}$, the circumferential distance around the wheel d, the inlet steady-state fluid density $\overline{\rho}_{-\infty}$, and the inlet steady-state fluid temperature $\overline{T}_{-\infty}$. In addition the subscripts (∞, $-\infty$) signify upstream and downstream flow variables. (The symbols used in this report are defined in appendix A.)

The continuity equation for the upstream and downstream flow fields is

$$\frac{\partial \rho_{\pm\infty}}{\partial t} + \frac{\partial}{\partial X_i}\left(U_{i,\pm\infty}\rho_{\pm\infty}\right) = 0 \tag{1}$$

where ρ, U_i, t, and X_i are the nondimensional density, velocity components, and time spacial coordinates, respectively. (See fig. 3 for definition of coordinate system.) In addition the use of repeated indices denotes summation with respect to the repeated index. The momentum equations for the flow fields are

$$\frac{\partial U_{i,\pm\infty}}{\partial t} + U_{j,\pm\infty}\frac{\partial U_{i\pm\infty}}{\partial X_j} = -\frac{1}{\rho_{\pm\infty}}\frac{\partial P_{\pm\infty}}{\partial X_i} \qquad i = 1,\ 2 \tag{2}$$

where $P_{\pm\infty}$ is the nondimensional pressure. The remaining field equations are the energy equation for an inviscid, nonconducting gas

$$\frac{\partial s_{\pm\infty}}{\partial t} + U_{i,\pm\infty}\frac{\partial s_{\pm\infty}}{\partial X_i} = 0 \tag{3}$$

and the equation of state

$$s_{\pm\infty} = \frac{1}{\gamma(\gamma-1)\overline{M}_{-\infty}^2}\ln\gamma\overline{M}_{-\infty}^2 P_{\pm\infty} - \frac{1}{(\gamma-1)\overline{M}_{-\infty}^2}\ln\rho_{\pm\infty} \tag{4}$$

(The entropy was nondimensionalized with respect to $\overline{T}_{-\infty}/\overline{q}_{-\infty}^2$.) The variables appearing in equations (3) and (4) are the entropy s; the ratio of specific heats γ; and the inlet steady-state relative Mach number $\overline{M}_{-\infty}$.

The preceding system of field equations is nonlinear. In this analysis they are cast into a system of linear equations with constant coefficients by expanding each equation to first order in terms of the amplitude of the perturbed variables. In the expansion process the zeroth-order terms are treated as constants. The resulting field equations are

$$\frac{\partial \tilde{\rho}_{\pm\infty}}{\partial t} + \bar{U}_{i,\pm\infty} \frac{\partial \tilde{\rho}_{\pm\infty}}{\partial X_i} + \bar{\rho}_{\pm\infty} \frac{\partial \tilde{U}_{i,\pm\infty}}{\partial X_i} = 0 \tag{5}$$

$$\frac{\partial \tilde{U}_{i,\pm\infty}}{\partial t} + \bar{U}_{j,\pm\infty} \frac{\partial \tilde{U}_{i,\pm\infty}}{\partial X_j} = -\frac{1}{\bar{\rho}_{\pm\infty}} \frac{\partial \tilde{P}_{\pm\infty}}{\partial X_i} \qquad i = 1,\ 2 \tag{6}$$

$$\frac{\partial \tilde{s}_{\pm\infty}}{\partial t} + \bar{U}_{i,\pm\infty} \frac{\partial \tilde{s}_{\pm\infty}}{\partial X_i} = 0 \tag{7}$$

$$\tilde{s}_{\pm\infty} = \frac{1}{\bar{M}_{-\infty}^2 \gamma} \frac{1}{\gamma - 1} \frac{\tilde{P}_{\pm\infty}}{\bar{P}_{\pm\infty}} \frac{1}{\gamma - 1} \frac{1}{\bar{M}_{-\infty}^2} \frac{\tilde{\rho}_{\pm\infty}}{\bar{\rho}_{\pm\infty}} \tag{8}$$

where the tilda denotes a time-dependent variable and the bar signifies a steady-state variable.

The present analysis assumes that there are no sources of entropy or vorticity upstream of the cascade. The upstream, unsteady velocity field must therefore be irrotational and hence is equal to the gradient of a potential function $\Phi_{-\infty}$, where

$$\tilde{U}_{i,-\infty} = \frac{\partial \tilde{\Phi}_{-\infty}}{\partial X_i} \qquad i = 1,\ 2 \tag{9}$$

The unsteady velocity field downstream of the cascade is expressed as

$$\tilde{U}_{i,\infty} = \frac{\partial \tilde{\Phi}_{\infty}}{\partial X_i} + \tilde{U}_{i,\infty}^{R} \qquad i = 1,\ 2 \tag{10}$$

where $\partial \tilde{\Phi}_{\infty} / \partial X_i$ represents the irrotational component of the field and $\tilde{U}_{i,\infty}^{R}$ its rotational component. The source of the rotation field is the vorticity shed by the oscillating airfoils. The governing equation for this vorticity field is derived (ref. 10) by taking the curl of equation (6), which yields

$$\frac{\partial \tilde{\xi}}{\partial t} + \bar{U}_{i,\infty} \frac{\partial \tilde{\xi}}{\partial X_i} \tag{11}$$

A solution of equation (11) is sought that is periodic in time and periodic along the cascade plane. This solution is given as

$$\tilde{\zeta} = E\, e^{-i\gamma_\infty X_1} e^{ik_2 X_2} e^{ikt} \tag{12}$$

where

$$\gamma_\infty = \frac{k + \bar{U}_{2,\infty} k_2}{\bar{U}_{1,\infty}} \tag{13}$$

$$k_2 = 2\pi m \tag{14}$$

(n is an integer)

$$k = \frac{\omega d}{\bar{q}_\infty} \tag{15}$$

and E is a complex constant. In reference 10 it is shown that a vorticity field has a vector potential associated with it. The relation between these two fields is given as

$$\nabla^2 \tilde{\Psi} = -\tilde{\zeta} \tag{16}$$

where ∇^2 is the Laplacian operator. In addition it is shown that the components of the rotational velocity field are

$$\frac{\partial \tilde{\Psi}}{\partial X_1} = -\tilde{U}_2^R \tag{17}$$

$$\frac{\partial \tilde{\Psi}}{\partial X_2} = \tilde{U}_1^R \tag{18}$$

The particular solution of equation (17) with the right side given by equation (16) is

$$\tilde{\Psi} = \frac{E}{\gamma_\infty^2 + k_2^2} e^{-i\gamma_\infty X_1} e^{ik_2 X_2} e^{ikt} \tag{19}$$

Thus from equations (17) and (18) the components of $\tilde{U}_i^R$ must be equal to

$$\tilde{U}_1^R = \frac{Eik_2}{\gamma_\infty^2 + k_2^2} e^{-i\gamma_\infty X_1} e^{ik_2 X_2} e^{ikt} \tag{20}$$

$$\tilde{U}_2^R = \frac{Ei\gamma_\infty}{\gamma_\infty^2 + k_2^2} e^{-i\gamma_\infty X_1} e^{ik_2 X_2} e^{ikt} \tag{21}$$

Solutions for the remaining flow variables are of the form

$$\tilde{\rho}_{\pm\infty} = \hat{\rho}_{\pm\infty} e^{\alpha X_1} e^{ik_2 X_2} e^{ikt} \tag{22}$$

$$\tilde{\Phi}_{\pm\infty} = C_{\pm\infty} e^{\alpha X_1} e^{ik_2 X_2} e^{ikt} \tag{23}$$

$$\tilde{s}_{-\infty} = 0 \tag{24}$$

$$\tilde{s}_{\infty} = S e^{\alpha X_1} e^{ik_2 X_2} e^{ikt} \tag{25}$$

$$\tilde{\rho}_{\pm\infty} = \hat{\rho}_{\pm\infty} e^{\alpha X_1} e^{ik_2 X_2} e^{ikt} \tag{26}$$

where $\hat{\rho}_{\pm\infty}$, $C_{\pm\infty}$, S, and $\hat{\rho}_{\pm\infty}$ are complex constants. Introducing these equations, along with equations (20) and (21), into the field equations yields

$$\tilde{\rho}_{-\infty} = -\overline{M}_{-\infty}^2 \left(ik + \overline{U}_{1,-\infty}\alpha_{-\infty} + i\overline{U}_{2,-\infty}k_2\right) C_{-\infty} e^{(\alpha_{-\infty}X_1 + ik_2X_2 + ikt)} \tag{27}$$

$$\tilde{\rho}_{\infty} = -\frac{\overline{\rho}_\infty}{\overline{q}_\infty^2}\overline{M}_\infty^2 \left[\left(ik + \overline{U}_{1,\infty}\alpha_\infty + i\overline{U}_{2,\infty}k_2\right) C_\infty e^{\alpha_\infty X_1} + (\gamma - 1)\overline{T}_\infty S e^{-i\gamma_\infty X_1}\right] e^{(ik_2X_2 + ikt)} \tag{28}$$

$$\tilde{\Phi}_{-\infty} = C_{-\infty} e^{(\alpha_{-\infty}X_1 + ik_2X_2 + ikt)} \tag{29}$$

$$\tilde{\Phi}_{\infty} = C_{\infty} e^{(\alpha_{\infty}X_1 + ik_2X_2 + ikt)} \tag{30}$$

$$\tilde{s}_{\infty} = S e^{(-i\gamma_\infty X_1 + ik_2X_2 + ikt)} \tag{31}$$

$$\tilde{P}_{-\infty} = -\left(ik + \overline{U}_{1,-\infty}\alpha_{-\infty} + \overline{U}_{2,-\infty}ik_2\right) C_{-\infty} e^{(\alpha_{-\infty}X_1 + ik_2X_2 + ikt)} \tag{32}$$

$$\tilde{P}_{\infty} = -\bar{\rho}_{\infty}\left(ik + \bar{U}_{1,\infty}\alpha_{\infty} + \bar{U}_{2,\infty}ik_2\right)C_{\infty}\, e^{(\alpha_{\infty}X_1 + ik_2X_2 + ikt)} \tag{33}$$

where

$$\alpha_{\pm\infty} = \frac{i\bar{U}_{1,\pm\infty}\delta_{\pm\infty}\bar{M}^2_{\pm\infty}(RQ)}{1 - \bar{M}^2_{\pm\infty}(RQ)\bar{U}^2_{1,\pm\infty}} \mp \frac{\sqrt{k_2^2\left[1 - \bar{M}^2_{\pm\infty}(RQ)\bar{U}^2_{1,\pm\infty}\right] - \delta^2_{\pm\infty}\bar{M}^2_{\pm\infty}(RQ)}}{1 - \bar{M}^2_{\pm\infty}(RQ)\bar{U}^2_{1,\pm\infty}} \tag{34}$$

$$\delta_{\pm\infty} = k + \bar{U}_{2,\pm\infty}k_2 \tag{35}$$

and

$$\left.\begin{aligned} RQ &= 1 \quad \text{for } X_1 < 0 \\ RQ &= \frac{\bar{q}^2_{-\infty}}{\bar{q}^2_{\infty}} \quad \text{for } X_1 > 0 \end{aligned}\right\} \tag{36}$$

In deriving these results it was assumed that the velocity field remained bounded at large distances from the cascade.

The solutions for the unsteady flow variables are functions of four complex constants. These constants are evaluated in the next section.

Boundary Conditions

The constants $C_{\pm\infty}$, S, and E that appear in the solutions derived in the preceding section are evaluated here from four boundary conditions at the deforming cascade plane. These boundary conditions are derived by modeling the oscillating cascade as a deforming actuator disk.

The first boundary condition requires the flow to be continuous across the deforming disk. The analytical form of this boundary condition is

$$\left(1 + \tilde{\rho}_{-\infty}\right)U^{Rel}_{n,-\infty} = \left(\bar{\rho}_{\infty} + \tilde{\rho}_{\infty}\right)U^{Rel}_{n,\infty} \quad \text{at } X_1 = 0 \tag{37}$$

where $U^{Rel}_{n,\pm\infty}$ represents the normal velocity components relative to the deforming disk. These velocity components to first order (i.e., small cascade-plane deflection) are equal to

$$U_{n,-\infty}^{Rel} = \overline{U}_{1,-\infty} + \frac{\partial \tilde{\Phi}_{-\infty}}{\partial X_1} - \frac{\partial \tilde{h}_1}{\partial t} - \overline{U}_{2,-\infty} \frac{\partial \tilde{h}_1}{\partial X_2} \tag{38}$$

$$U_{n,\infty}^{Rel} = \overline{U}_{1,\infty} + \frac{\partial \tilde{\Phi}_{\infty}}{\partial X_1} - \frac{\partial \tilde{h}_1}{\partial t} - \overline{U}_{2,\infty} \frac{\partial \tilde{h}_1}{\partial X_2} + \frac{\partial \tilde{\Psi}}{\partial X_2} \tag{39}$$

where $\tilde{h}_1$ is the displacement of the disk from its mean position in the axial (X_1) direction (fig. 4). The assumed analytical form for $\tilde{h}_1$ is

$$\tilde{h}_1 = h_1 e^{ik_2 X_2} e^{ikt} \tag{40}$$

where h_1 is a real constant. Substituting equations (38) to (40) into equation (37) yields, to first order,

$$\overline{U}_{-\infty} = \overline{\rho}_{\infty} \overline{U}_{\infty} \qquad \text{at } X_1 = 0 \tag{41}$$

and

$$\tilde{\rho}_{-\infty} \overline{U}_{1,-\infty} - \tilde{\rho}_{\infty} \overline{U}_{1,\infty} + \frac{\partial \tilde{\Phi}_{\infty}}{\partial X_1} - \overline{\rho}_{\infty} \left(\frac{\partial \tilde{\Phi}_{\infty}}{\partial X_1} + \frac{\partial \tilde{\Psi}}{\partial X_2} \right)$$

$$= h_1 \left(ik + \overline{U}_{2,-\infty} ik_2 - \overline{\rho}_{\infty} ik - \overline{\rho}_{\infty} \overline{U}_{2,\infty} ik_2 \right) e^{ik_2 X_2} e^{ikt} \qquad \text{at } X_1 = 0 \tag{42}$$

Introducing the expressions derived in the preceding section into equation (42) yields the algebraic equation

$$\alpha_{11} C_{-\infty} + \alpha_{12} C_{\infty} + \alpha_{13} E + \alpha_{14} S = R_1 \tag{43}$$

where the constants α_{11}, α_{12}, α_{13}, α_{14}, and R_1 are defined in appendix B.

The next boundary condition requires the total enthalpy with respect to the deforming actuator disk to be locally conserved across the disk. The equivalent mathematical statement is

$$\frac{1}{\gamma - 1} \frac{1}{\overline{M}_{-\infty}^2} T_{-\infty} + \frac{1}{2} q_{-\infty}^{2,Rel} = \frac{1}{\gamma - 1} \frac{1}{\overline{M}_{-\infty}^2} T_{\infty} + \frac{1}{2} q_{\infty}^{2,Rel} \qquad \text{at } X_1 = 0 \tag{44}$$

where $T_{\pm\infty}$ is the upstream and downstream gas temperature and $q_{\pm\infty}^{Rel}$ is the magni-

tude of the relative velocity approaching and leaving the disk. The expressions for $q_{\pm\infty}^{Rel}$ are

$$q_{-\infty}^{Rel} = \left[\left(\overline{U}_{1,-\infty} + \frac{\partial\tilde{\Phi}_{-\infty}}{\partial X_1} - \frac{\partial\tilde{h}_1}{\partial t}\right)^2 + \left(\overline{U}_{2,\infty} + \frac{\partial\tilde{\Phi}_{-\infty}}{\partial X_2} - \frac{\partial\tilde{h}_2}{\partial t}\right)^2\right]^{1/2} \tag{45}$$

$$q_{\infty}^{Rel} = \left[\left(\overline{U}_{1,\infty} + \frac{\partial\tilde{\Phi}_{\infty}}{\partial X_1} + \frac{\partial\tilde{\Psi}}{\partial X_2} - \frac{\partial\tilde{h}_1}{\partial t}\right)^2 + \left(\overline{U}_{2,\infty} + \frac{\partial\tilde{\Phi}_{\infty}}{\partial X_2} - \frac{\partial\tilde{\Psi}}{\partial X_1} - \frac{\partial\tilde{h}_2}{\partial t}\right)^2\right]^{1/2} \tag{46}$$

where $\tilde{h}_2$ is the local displacement of the cascade in the tangential (X_2) direction (fig. 4). The analytical form assumed for $\tilde{h}_2$ is

$$\tilde{h}_2 = h_2 e^{ik_2X_2} e^{ikt} \tag{47}$$

where h_2 is the complex amplitude of the displacement. Combining equations (45) and (46) with equation (44) and expanding to first order yield

$$\frac{1}{\gamma - 1}\frac{\overline{T}_{-\infty}}{\overline{M}_{-\infty}^2} + \frac{1}{2}\left(\overline{U}_{1,-\infty}^2 + \overline{U}_{2,-\infty}^2\right) = \frac{1}{\gamma - 1}\frac{\overline{T}_{\infty}}{\overline{M}_{-\infty}^2} + \frac{1}{2}\left(\overline{U}_{1,\infty}^2 + \overline{U}_{2,\infty}^2\right) \quad \text{at } X_1 = 0 \tag{48}$$

and

$$\frac{1}{\gamma - 1}\frac{1}{\overline{M}_{-\infty}^2}\tilde{T}_{-\infty} + \overline{U}_{1,-\infty}\left(\frac{\partial\tilde{\Phi}_{-\infty}}{\partial X_1} - \frac{\partial\tilde{h}_1}{\partial t}\right) + \overline{U}_{2,-\infty}\left(\frac{\partial\tilde{\Phi}_{-\infty}}{\partial X_2} - \frac{\partial\tilde{h}_2}{\partial t}\right) = \frac{1}{\gamma - 1}\frac{1}{\overline{M}_{-\infty}^2}\tilde{T}_{\infty}$$

$$+ \overline{U}_{1,\infty}\left(\frac{\partial\tilde{\Phi}_{\infty}}{\partial X_1} + \frac{\partial\tilde{\Psi}}{\partial X_2} - \frac{\partial\tilde{h}_1}{\partial t}\right) + \overline{U}_{2,\infty}\left(\frac{\partial\tilde{\Phi}_{\infty}}{\partial X_2} - \frac{\partial\tilde{\Psi}}{\partial X_1} - \frac{\partial\tilde{h}_2}{\partial t}\right) \quad \text{at } X_1 = 0 \tag{49}$$

The local, total enthalpy change across the actuator disk as observed with respect to the X_1, X_2 coordinate system is

$$\frac{1}{\gamma - 1}\frac{\tilde{T}_{0,-\infty} - \tilde{T}_{0,\infty}}{\overline{M}^2_{-\infty}} = \frac{1}{\gamma - 1}\frac{1}{\overline{M}^2_{-\infty}}\left(\tilde{T}_{-\infty} - \tilde{T}_{\infty}\right) + \overline{U}_{1,-\infty}\frac{\partial\tilde{\Phi}_{-\infty}}{\partial X_1} - \overline{U}_{1,\infty}\left(\frac{\partial\tilde{\Phi}_{\infty}}{\partial X_1} + \frac{\partial\tilde{\Psi}}{\partial X_2}\right)$$

$$+ \overline{U}_{2,-\infty}\frac{\partial\tilde{\Phi}_{-\infty}}{\partial X_2} - \overline{U}_{2,\infty}\left(\frac{\partial\tilde{\Phi}_{\infty}}{\partial X_2} - \frac{\partial\tilde{\Psi}}{\partial X_1}\right) \quad \text{at } X_1 = 0 \tag{50}$$

In deriving equation (50), variables higher than first order have been neglected. Combining equation (50) with equation (49) yields

$$\frac{1}{\gamma - 1}\frac{\tilde{T}_{0,-\infty} - \tilde{T}_{0,\infty}}{\overline{M}^2_{-\infty}} = \left(\overline{U}_{1,-\infty} - \overline{U}_{1,\infty}\right)\frac{\partial\tilde{h}_1}{\partial t} + \left(\overline{U}_{2,-\infty} - \overline{U}_{2,\infty}\right)\frac{\partial\tilde{h}_2}{\partial t} \quad \text{at } X_1 = 0 \tag{51}$$

Equation (51) shows that, if the steady aerodynamic force is a finite quantity, the contribution of these forces to the total enthalpy rise across the disk is a first-order quantity. Combining equation (51) with equation (C15) of appendix C produces the second boundary condition

$$\frac{\partial\left(\tilde{U}_{2,-\infty} - \tilde{U}_{2,\infty}\right)}{\partial t} - \overline{U}_{1,\infty}\tilde{\xi} = -\overline{T}_{\infty}\frac{\partial\tilde{s}_{\infty}}{\partial X_2} - \left(\overline{U}_{1,-\infty} - \overline{U}_{1,\infty}\right)\frac{\partial^2\tilde{h}_1}{\partial X_2 \partial t}$$

$$- \left(\overline{U}_{2,-\infty} - \overline{U}_{2,\infty}\right)\frac{\partial^2\tilde{h}_2}{\partial X_2 \partial t} \quad \text{at } X_1 = 0 \tag{52}$$

Substituting the solutions for the field variables into equation (52) yields

$$\alpha_{21}C_{-\infty} + \alpha_{22}C_{\infty} + \alpha_{23}E + \alpha_{24}S = R_2 \tag{53}$$

The coefficients in this equation are defined in appendix B.

The third boundary condition requires that the local exit flow angle relative to the defoming actuator disk be specified. This angle is defined by the equation

$$\tan\beta_{\infty} = \frac{\overline{U}_{2,\infty} + \frac{\partial\tilde{\Phi}_{\infty}}{\partial X_2} - \frac{\partial\tilde{\Psi}}{\partial X_1} - \frac{\partial\tilde{h}_2}{\partial t}}{\overline{U}_{1,\infty} + \frac{\partial\tilde{\Phi}_{\infty}}{\partial X_1} + \frac{\partial\tilde{\Psi}}{\partial X_2} - \frac{\partial\tilde{h}_1}{\partial t}} \quad \text{at } X_1 = 0 \tag{54}$$

Expanding the right and left sides of this equation to first order yields

$$\tan \overline{\beta}_{\infty} = \frac{\overline{U}_{2,\infty}}{\overline{U}_{1,\infty}} \qquad \text{at } X_1 = 0 \tag{55}$$

and

$$\tilde{\beta}_{\infty} = \frac{1}{\overline{U}_{1,\infty}} \left(\frac{\partial \tilde{\Phi}_{\infty}}{\partial X_2} - \frac{\partial \tilde{\Psi}}{\partial X_1} - \frac{\partial \tilde{h}_2}{\partial t} \right) \frac{1}{\sec^2 \overline{\beta}_{\infty}} - \frac{\overline{U}_{2,\infty}}{\overline{U}^2_{1,\infty}} \left(\frac{\partial \tilde{\Phi}_{\infty}}{\partial X_1} + \frac{\partial \tilde{\Psi}}{\partial X_2} - \frac{\partial \tilde{h}_1}{\partial t} \right) \frac{1}{\sec^2 \overline{\beta}_{\infty}} \qquad \text{at } X_1 = 0 \tag{56}$$

where the local, perturbed exit flow angle $\tilde{\beta}_{\infty}$ is defined as

$$\tilde{\beta}_{\infty} = \beta_{\infty} - \overline{\beta}_{\infty} \tag{57}$$

The present analysis assumes that the local, relative exit flow angle can be related to the local, relative inlet flow field (i.e., flow properties measured with respect to the deforming disk) through a quasi-steady deviation-angle correlation of the form

$$\delta = g\left(\alpha,\ M_{-\infty},\ \sigma,\ \theta'\right) \tag{58}$$

where α is the local, relative incidence angle, $M_{-\infty}$ is the local, relative inlet Mach number, σ is the local solidity of the deformed cascade, and θ' is the local stagger angle measured from the normal to the leading-edge plane (fig. 4). The local, relative incidence angle is related to the local, relative inlet flow angle $\beta'_{-\infty}$ measured from the normal to the leading-edge plane by the equation

$$\alpha = \beta'_{-\infty} - \theta' - \delta_{m_1} \tag{59}$$

The variable δ_{m_1} in this equation is the angle between the chord line and the tangent to the camber line at the leading edge. The corresponding relation for the local deviation angle is

$$\delta = \beta'_{\infty} - \theta' - \delta_{m_2} \tag{60}$$

where β'_{∞} is the local, relative exit flow angle measured from the normal to the trailing-edge plane and δ_{m_2} is the angle between the chord line and the tangent to the

camber line at the trailing edge. If the leading-edge plane of the cascade is deforming in time, the local inlet and exit relative flow angles $\beta_{-\infty}$ and β_{∞} measured with respect to the X_1-axis deviate from $\beta'_{-\infty}$ and β'_{∞} by the angle $\tan^{-1}\left(\partial\tilde{h}_1/\partial X_2\right)$. For small displacements, $\beta_{-\infty}$ and β_{∞} are

$$\beta_{-\infty} = \beta'_{-\infty} + \frac{\partial\tilde{h}_1}{\partial X_2} \tag{61}$$

$$\beta_{\infty} = \beta'_{\infty} + \frac{\partial\tilde{h}_1}{\partial X_2} \tag{62}$$

Similarly the angle θ between the chord line and the axial direction (fig. 4) is related to the local stagger angle θ' by the equation

$$\theta = \theta' + \frac{\partial\tilde{h}_1}{\partial X_2} \tag{63}$$

Combining equations (58) to (63) produces the results

$$\alpha = \beta_{-\infty} - \theta - \delta_{m_1} \tag{64}$$

$$\delta = \beta_{\infty} - \theta - \delta_{m_2} \tag{65}$$

and

$$\beta_{\infty} = \theta + \delta_{m_2} + g\left[\alpha\left(\beta_{-\infty},\ \theta,\ \delta_{m_1}\right),\ M_{-\infty},\ \sigma,\ \theta'\left(\theta,\ \frac{\partial\tilde{h}_1}{\partial X_2}\right)\right] \tag{66}$$

In the present analysis the variables in equation (66) that are a function of the vibratory motion are β_{∞}, $\beta_{-\infty}$, $M_{-\infty}$, σ, and $\partial\tilde{h}_1/\partial X_2$. Expanding equation (66) to first order with respect to these variables yields

$$\bar{\beta}_{\infty} = \theta + \delta_{m_2} + g\left(\bar{\alpha},\ \bar{M}_{-\infty},\ \bar{\sigma},\ \bar{\theta}'\right) \tag{67}$$

and

$$\tilde{\beta}_{\infty} = \frac{\partial g}{\partial \beta_{-\infty}} \left(\beta_{-\infty} - \overline{\beta}_{-\infty} \right) + \frac{\partial g}{\partial M_{-\infty}} \left(M_{-\infty} - \overline{M}_{-\infty} \right) + \frac{\partial g}{\partial \sigma} (\sigma - \overline{\sigma}) + \frac{\partial g}{\partial \left(\frac{\partial \tilde{h}_1}{\partial X_2} \right)} \frac{\partial \tilde{h}_1}{\partial X_2} \tag{68}$$

The local, relative inlet flow angle and the local, relative Mach number are defined by the equations

$$\tan \beta_{-\infty} = \frac{\overline{U}_{2,-\infty} + \frac{\partial \tilde{\Phi}_{-\infty}}{\partial X_2} - \frac{\partial \tilde{h}_2}{\partial t}}{\overline{U}_{1,-\infty} + \frac{\partial \tilde{\Phi}_{-\infty}}{\partial X_1} - \frac{\partial \tilde{h}_1}{\partial t}} \quad \text{at } X_1 = 0 \tag{69}$$

$$M_{-\infty} = \frac{q^{Rel}_{-\infty}}{\sqrt{\frac{\gamma P_{-\infty}}{\rho_{-\infty}}}} \quad \text{at } X_1 = 0 \tag{70}$$

Expanding both these equations to first order yields

$$\tan \overline{\beta}_{-\infty} = \frac{\overline{U}_{2,-\infty}}{\overline{U}_{1,-\infty}} \tag{71}$$

$$\beta_{-\infty} - \overline{\beta}_{-\infty} \equiv \tilde{\beta}_{-\infty} = \frac{1}{\overline{U}_{1,-\infty} \sec^2 \overline{\beta}_{-\infty}} \left(\frac{\partial \tilde{\Phi}_{-\infty}}{\partial X_2} - \frac{\partial \tilde{h}_2}{\partial t} \right)$$

$$- \frac{\overline{U}_{2,\infty}}{\overline{U}^2_{1,-\infty} \sec^2 \overline{\beta}_{-\infty}} \left(\frac{\partial \tilde{\Phi}_{-\infty}}{\partial X_1} - \frac{\partial \tilde{h}_1}{\partial t} \right) \quad \text{at } X_1 = 0 \tag{72}$$

$$\overline{M}_{-\infty} = \frac{1}{\sqrt{\gamma \overline{P}_{-\infty}}} \tag{73}$$

$$M_{-\infty} - \overline{M}_{-\infty} \equiv \widetilde{M}_{-\infty} = \overline{M}_{-\infty} \widetilde{q}^{Rel}_{-\infty} - \frac{1}{2} \overline{M}_{-\infty} \frac{\widetilde{P}_{-\infty}}{\overline{P}_{-\infty}} + \frac{1}{2} \overline{M}_{-\infty} \widetilde{\rho}_{-\infty} \tag{74}$$

where

$$\widetilde{q}^{Rel}_{-\infty} = \overline{U}_{1,-\infty} \left(\frac{\partial \widetilde{\Phi}_{-\infty}}{\partial X_1} - \frac{\partial \widetilde{h}_1}{\partial t} \right) + \overline{U}_{2,-\infty} \left(\frac{\partial \widetilde{\Phi}_{-\infty}}{\partial X_2} - \frac{\partial \widetilde{h}_2}{\partial t} \right) \tag{75}$$

From figure 4, the local solidity of the deformed cascade is

$$\sigma = \frac{\overline{\sigma} \cos \left(\tan^{-1} \frac{\partial \widetilde{h}_1}{\partial X_2} \right)}{1 + h_2 N \cos \left(\tan^{-1} \frac{\partial \widetilde{h}_1}{\partial X_2} \right) e^{(ik_2 X_2 + ikt)}} \tag{76}$$

Expanding equation (76) to first order yields

$$\sigma - \overline{\sigma} \equiv \widetilde{\sigma} = -\overline{\sigma} h_2 N \left(e^{ik_2/N} - 1 \right) e^{(ik_2 X_2 + ikt)} \tag{77}$$

which for small interblade phase angles $\left(|k_2/N| << 1 \right)$ becomes

$$\widetilde{\sigma} = -\overline{\sigma} h_2 i k_2 \, e^{(ik_2 X_2 + ikt)} = -\frac{\partial \widetilde{h}_2}{\partial X_2} \overline{\sigma} \tag{78}$$

Introducing equations (72), (74), and (78) into the right side of equation (68) and replacing the left side with equation (56) produce the third boundary condition

$$\frac{1}{\overline{U}_{1,\infty}\sec^2\overline{\beta}_\infty}\left(\frac{\partial\tilde{\Phi}_\infty}{\partial X_2}-\frac{\partial\tilde{\Psi}}{\partial X_1}-\frac{\partial\tilde{h}_2}{\partial t}\right)-\frac{\overline{U}_{2,\infty}}{\overline{U}^2_{1,\infty}\sec^2\overline{\beta}_\infty}\left(\frac{\partial\tilde{\Phi}_\infty}{\partial X_1}+\frac{\partial\tilde{\Psi}}{\partial X_2}-\frac{\partial\tilde{h}_1}{\partial t}\right)$$

$$=\frac{\partial g}{\partial\beta_{-\infty}}\left[\frac{1}{\overline{U}_{1,-\infty}\sec^2\overline{\beta}_{-\infty}}\left(\frac{\partial\tilde{\Phi}_\infty}{\partial X_2}-\frac{\partial\tilde{h}_2}{\partial t}\right)-\frac{\overline{U}_{2,-\infty}}{\overline{U}^2_{1,-\infty}\sec^2\overline{\beta}_{-\infty}}\left(\frac{\partial\tilde{\Phi}_{-\infty}}{\partial X_1}-\frac{\partial\tilde{h}_1}{\partial t}\right)\right]$$

$$+\frac{\partial g}{\partial M_{-\infty}}\left[\overline{M}_{-\infty}\overline{U}_{1,-\infty}\left(\frac{\partial\tilde{\Phi}_{-\infty}}{\partial X_1}-\frac{\partial\tilde{h}_1}{\partial t}\right)+\overline{M}_{-\infty}\overline{U}_{2,-\infty}\left(\frac{\partial\tilde{\Phi}_{-\infty}}{\partial X_2}-\frac{\partial\tilde{h}_2}{\partial t}\right)-\frac{1}{2}\frac{\overline{M}_{-\infty}}{\overline{P}_{-\infty}}\tilde{P}_{-\infty}+\frac{1}{2}\overline{M}_{-\infty}\tilde{\rho}_{-\infty}\right]$$

$$-\frac{\partial g}{\partial\sigma}\frac{\partial\tilde{h}_2}{\partial X_2}\overline{\sigma}+\frac{\partial g}{\partial\left(\frac{\partial h_1}{\partial X_2}\right)}\frac{\partial\tilde{h}_1}{\partial X_2}\qquad\text{at } X_1=0 \tag{79}$$

Introducing the solutions for the field variables into this boundary condition transforms it into the equation

$$\alpha_{31}C_{-\infty}+\alpha_{32}C_\infty+\alpha_{33}E+\alpha_{34}S=R_3 \tag{80}$$

where the coefficients of the complex constants are defined in appendix B.

The last boundary condition specifies the local entropy that is generated as the fluid passes through the cascade. The loss associated with the local entropy rise is defined in terms of a loss coefficient defined as

$$\chi=\frac{P^{Rel}_{0,-\infty}-P^{Rel}_{0,\infty}}{\frac{1}{2}\rho_{-\infty}q^{2,Rel}_{-\infty}} \tag{81}$$

The variable $P^{Rel}_{0,-\infty}-P^{Rel}_{0,\infty}$ in this equation represents the local total-pressure loss measured relative to the deforming actuator disk. The entropy rise across the disk is related to this quantity by the equation of state

$$P_{0,-\infty}^{Rel} - P_{0,\infty}^{Rel} = P_{0,-\infty}^{Rel}\left(1 - e^{-\gamma\overline{M}_{-\infty}^2 s_\infty}\right) \tag{82}$$

Combining equation (81) with equation (82) and solving for s_∞ yield

$$s_\infty = -\frac{1}{\gamma\overline{M}_{-\infty}^2}\,\ell n\left(1 - \frac{1}{2}\,\frac{\rho_{-\infty} q_{-\infty}^{2,\,Rel}\chi}{P_{0,-\infty}}\right) \tag{83}$$

The present analysis assumes that the local loss coefficient χ is related to the local inlet flow field, as observed with respect to the deforming disk, by a quasi-steady relation of the form

$$\chi = \chi(\alpha,\ M_{-\infty},\ \sigma,\ \theta') \tag{84}$$

The dependent variables in this equation are identical to those that appeared in equation (58). Introducing equation (84) into equation (83) and expanding the resulting expression to first order yield

$$\overline{s}_\infty = -\frac{1}{\gamma\overline{M}_{-\infty}^2}\,\ln\left(1 - \frac{1}{2}\,\frac{\overline{\chi}}{\overline{P}_{0,-\infty}}\right) \tag{85}$$

and

$$\tilde{s} = -\frac{e^{\overline{s}\gamma\overline{M}_{-\infty}^2}}{\gamma\overline{M}_{-\infty}^2}\left[\frac{1}{2}\,\frac{\overline{\chi}}{\overline{P}_{0,-\infty}}\,\frac{\tilde{P}_{0,-\infty}^{Rel}}{\overline{P}_{0,-\infty}} - \frac{1}{2}\,\frac{\delta\left(\rho_{-\infty} q_{-\infty}^{2,\,Rel}\chi\right)}{\overline{P}_{0,-\infty}}\right] \quad \text{at } X_1 = 0 \tag{86}$$

where $\tilde{P}_{0,-\infty}^{Rel}$ is the local, perturbed inlet total pressure measured relative to the deforming disk. This variable may be related to the local, perturbed inlet pressure $\tilde{P}_{-\infty}$ and the local, perturbed inlet Mach number $\tilde{M}_{-\infty}$ by expanding the definition of $P_{0,-\infty}$

$$P_{0,-\infty} = p_{-\infty}\left(1 + \frac{\gamma - 1}{2}\,M_{-\infty}^{2,\,Rel}\right)^{\gamma/(\gamma-1)} \tag{87}$$

to first order:

$$\overline{P}_{0,-\infty} = \overline{p}_{-\infty}\left(1 + \frac{\gamma - 1}{2}\overline{M}^2_{-\infty}\right)^{\gamma/(\gamma-1)} \tag{88}$$

$$\tilde{P}^{Rel}_{0,-\infty} = \tilde{p}_{-\infty}\frac{\overline{p}_{0,-\infty}}{\overline{P}_{-\infty}} + \overline{p}_{-\infty}\gamma\overline{M}_{-\infty}\left(\frac{\overline{P}_{0,-\infty}}{\overline{P}_{-\infty}}\right)^{1/\gamma}\tilde{M}_{-\infty} \tag{89}$$

The remaining perturbed quantity in equation (86) is equal to

$$\delta\left(\rho_{-\infty}q^{2,Rel}_{-\infty}\chi\right) = \overline{\chi}\tilde{\rho}_{-\infty} + 2\overline{\chi}\tilde{q}^{Rel}_{-\infty} + \left[\frac{\partial\chi}{\partial\beta_{-\infty}}\tilde{\beta}_{-\infty} + \frac{\partial\chi}{\partial M_{-\infty}}\tilde{M}_{-\infty} + \frac{\partial\chi}{\partial\sigma}\tilde{\sigma} + \frac{\partial\chi}{\partial\left(\frac{\partial\tilde{h}_1}{\partial X_2}\right)}\frac{\partial\tilde{h}_1}{\partial X_2}\right] \tag{90}$$

where $\tilde{\beta}_{-\infty}$, $\tilde{M}_{-\infty}$, $\tilde{q}^{Rel}_{-\infty}$, and $\tilde{\sigma}$ are defined by equations (72), (74), (75), and (78). Introducing the two preceding equations into equation (86) yields the fourth boundary condition

$$\tilde{s} = -\frac{e^{\frac{\overline{s}\gamma\overline{M}^2_{-\infty}}{2\gamma\overline{M}^2_{-\infty}}}}{2\gamma\overline{M}^2_{-\infty}}\frac{\overline{\chi}}{\overline{P}_{0,-\infty}}\left\{\frac{\tilde{P}_{-\infty}}{\overline{P}_{-\infty}} - \tilde{\rho}_{-\infty} - 2\tilde{q}^{Rel}_{-\infty} + \gamma M_{-\infty}\left(\frac{\overline{P}_{0,-\infty}}{\overline{P}_{-\infty}}\right)^{1/(\gamma-1)}\tilde{M}_{-\infty}\right.$$

$$\left. - \left[\frac{\partial \ln X}{\partial\beta_{-\infty}}\tilde{\beta}_{-\infty} + \frac{\partial \ln X}{\partial M_{-\infty}}\tilde{M}_{-\infty} + \frac{\partial \ln X}{\partial\sigma}\tilde{\sigma} + \frac{\partial \ln X}{\partial\left(\frac{\partial\tilde{h}_1}{\partial X_2}\right)}\frac{\partial\tilde{h}_1}{\partial X_2}\right]\right\} \quad \text{at } X_1 = 0 \tag{91}$$

Substituting the solution for the flow variables into this last boundary condition reduces it to

$$\alpha_{41}C_{-\infty} + \alpha_{42}C_{\infty} + \alpha_{43}E + \alpha_{44}S = R_4 \tag{92}$$

where the coefficients α_{41}, α_{42}, α_{43}, α_{44}, and R_4 are defined in appendix B.

The four boundary conditions applied in the present analysis have produced a system of nonlinear algebraic equations for the steady flow fields and four linear algebraic equations for the complex constants $C_{\pm\infty}$, E, and S. The steady flow equations are used to relate the steady downstream flow variables to the cascade geometry and the steady inlet flow properties. These relations are incorporated into the algebraic equation for $C_{\pm\infty}$, E, and S and render them independent of the downstream steady flow properties. The solutions for $C_{\pm\infty}$, E, and S are combined with equations (19), (29), (30), and (31) and are used in the next section to calculate the unsteady aerodynamic force acting on the cascade.

Aerodynamic Force

The aerodynamic force acting on a deforming cascade is obtained by considering the flow field through a control volume that is fixed to a cascade passage (fig. 3). The present analysis assumes that the relative motion between neighboring airfoils, a measure of which is the interblade phase angle, is small and that the reduced frequency of this motion is also small. The first assumption implies that the spatial variations of the flow variables across a cascade passage are small and thus can be neglected. The low-frequency assumption suggests that the rate of change of mass and momentum within the control volume is smaller than the net mass and momentum flux across the control volume surface and thus can also be neglected in the present analysis. Based on these considerations the momentum equation for the control volume illustrated in figure 3 can be written as

$$F_i = (p_{\infty} - p_{-\infty})n_i\tau + W^{Rel}(U_{i,\infty} - U_{i,-\infty}) \tag{93}$$

where F_i is the force exerted by the airfoils on the control volume, τ is the pitch of the cascade, W^{Rel} is the mass flow exiting the control volume, and n_1 is the unit vector normal to the exit plane of the control volume. Expanding equation (93) to first order yields

$$\overline{F}_i = \left(\overline{p}_{\infty} - \overline{p}_{-\infty}\right)\overline{n}_i\overline{\tau} + \overline{W}\left(\overline{U}_{i,\infty} - \overline{U}_{i,-\infty}\right) \tag{94}$$

and

$$\tilde{F}_i = \left(\tilde{p}_\infty - \tilde{p}_{-\infty}\right)\bar{n}_i\bar{\tau} + \left(\bar{p}_\infty - \bar{p}_{-\infty}\right)\tilde{n}_i\bar{\tau}$$

$$+ \left(\bar{p}_\infty - \bar{p}_{-\infty}\right)\bar{n}_i\tilde{\tau} + \tilde{W}^{Rel}\left(\bar{U}_{i,\infty} - \bar{U}_{i,-\infty}\right) + \bar{W}\left(\tilde{U}_{i,\infty} - \tilde{U}_{i,-\infty}\right) \tag{95}$$

The mass flow exiting the control volume is

$$W^{Rel} = \rho_\infty \tau \left(\bar{U}_{i,\infty} + \tilde{U}_{i,\infty} - \frac{\partial \tilde{h}_i}{\partial t}\right) n_i \tag{96}$$

which, expanded to first order, becomes

$$\bar{W} = \bar{\rho}_\infty \bar{\tau} \bar{U}_{i,\infty} \bar{n}_i \tag{97}$$

$$\tilde{W}^{Rel} = \tilde{\rho}_\infty \bar{\tau} \bar{U}_{i,\infty} \bar{n}_i + \bar{\rho}_\infty \tilde{\tau} \bar{U}_{i,\infty} \bar{n}_i + \bar{\rho}_\infty \bar{\tau} \left(\tilde{U}_i - \frac{\partial \tilde{h}_i}{\partial t}\right) \bar{n}_i + \bar{\rho}_\infty \bar{\tau} \bar{U}_{i,\infty} \tilde{n}_i \tag{98}$$

For the airfoil displacements under consideration in this analysis, the components of the unit vector n_i are

$$\tilde{n}_1 = \cos\left[\tan^{-1}\left(\frac{\partial \tilde{h}_1}{\partial X_2}\right)\right] \tag{99}$$

$$\tilde{n}_2 = -\sin\left[\tan^{-1}\left(\frac{\partial \tilde{h}_1}{\partial X_2}\right)\right] \tag{100}$$

Expanding both of these equations to first order yields

$$\left.\begin{aligned} \bar{n}_1 &= 1 \\ \bar{n}_2 &= 0 \end{aligned}\right\} \tag{101}$$

$$\left.\begin{aligned} \tilde{n}_1 &= 0 \\ \tilde{n}_2 &= -\frac{\partial \tilde{h}_1}{\partial X_2} \end{aligned}\right\} \tag{102}$$

Introducing these relations into equations (97) and (98) reduces them to

$$\overline{W} = \overline{\rho}_\infty \overline{\tau} \overline{U}_{1,\infty} \tag{103}$$

and

$$\tilde{W}^{Rel} = \tilde{\rho}_\infty \overline{\tau} \overline{U}_{1,\infty} + \overline{\rho}_\infty \tilde{\tau} \overline{U}_{1,\infty} + \overline{\rho}_\infty \overline{\tau} \left(\tilde{U}_1 - \frac{\partial \tilde{h}_1}{\partial t} \right) - \overline{\rho}_\infty \overline{\tau} \overline{U}_{2,\infty} \frac{\partial \tilde{h}_1}{\partial X_2} \tag{104}$$

In addition if equations (101) and (102) are introduced into equation (95), the components of the unsteady aerodynamic force become

$$\tilde{F}_1 = \left(\tilde{p}_\infty - \tilde{p}_{-\infty} \right) \overline{\tau} + \left(\overline{p}_\infty - \overline{p}_{-\infty} \right) \tilde{\tau} + \tilde{W}^{Rel} \left(\overline{U}_{1,\infty} - \overline{U}_{1,-\infty} \right) + \overline{W} \left(\tilde{U}_{1,\infty} - \tilde{U}_{1,-\infty} \right) \tag{105}$$

$$\tilde{F}_2 = -\left(\overline{p}_\infty - \overline{p}_{-\infty} \right) \overline{\tau} \frac{\partial h_1}{\partial X_2} + \tilde{W}^{Rel} \left(\overline{U}_{2,\infty} - \overline{U}_{2,-\infty} \right) + \overline{W} \left(\tilde{U}_{2,\infty} - \tilde{U}_{2,-\infty} \right) \tag{106}$$

The work done by the aerodynamic force on an airfoil over a cycle of motion is equal to

$$W_{Aero} = -\frac{1}{2} \mathcal{R}e \left[\int_0^{2\pi/k} \left(\tilde{F}_1 \frac{\partial \tilde{h}_1^*}{\partial t} + \tilde{F}_2 \frac{\partial \tilde{h}_2^*}{\partial t} \right) dt \right] \tag{107}$$

where $\mathcal{R}e[\ ]$ denotes the real part of the expression and the asterisk superscript signifies the complex conjugate of the variable. Inserting equations (40) and (47) into equation (107) and evaluating the integral yield

$$W_{Aero} = -\mathcal{I}m \left(\tilde{F}_i \tilde{h}_i^* \right) \tag{108}$$

where $\mathcal{Im}$ [ ] represents the imaginary part of the expression within the brackets in equation (107). At the onset of flutter the aerodynamic work per cycle is equal to the mechanical energy dissipated over a cycle. If the mechanical dissipative force is proportional to the velocity of the airfoil, the mechanical energy dissipated over a cycle of motion is

$$W_D = \frac{C}{2\overline{\rho}_{-\infty} q_{-\infty} d} \mathcal{Re}\left[\int_0^{2\pi/k} \left(\frac{\partial \tilde{h}_1}{\partial t}\frac{\partial \tilde{h}_1^*}{\partial t} + \frac{\partial \tilde{h}_2}{\partial t}\frac{\partial \tilde{h}_2^*}{\partial t}\right) dt\right] \tag{109}$$

where the damping coefficient C is defined as

$$C = \frac{\delta M_b}{2\pi} k \frac{\overline{q}_{-\infty}}{d} \tag{110}$$

The variable δ in this equation is the log decrement of the mechanical damping, and M_b is the mass per unit length of a rotor blade. This variable is defined as

$$M_b = K\rho_b \tau c \tag{111}$$

where K is a constant of proportionality, ρ_b is the blade density, τ is the average thickness of the blade, and c is its average chord length. Introducing this equation along with equation (110) into the integrated form of equation (109) yields

$$W_D = 2\delta K\left(\frac{\rho_b}{\overline{\rho}_{-\infty}}\right)\frac{\tau}{c} k_b^2 \left(\tilde{h}_1\tilde{h}_1^* + \tilde{h}_2\tilde{h}_2^*\right) \tag{112}$$

Equating equation (112) with equation (108) and solving for δ establishes the minimum level of mechanical damping required for stability at an operating point as

$$\delta_{Onset} = -\frac{\pi}{2K}\left(\frac{\rho_{-\infty}}{\rho_b}\right)\frac{1}{\frac{\tau}{c}} \frac{1}{k_b^2\left(h_1 h_1^* + h_2 h_2^*\right)} \mathrm{Min}_{k_2}\left[\mathcal{Im}\left(\tilde{F}_2\tilde{h}_2^*\right)\right] \tag{113}$$

The symbol Min_{k_2} denotes the minimum value of the function with respect to k_2. If the available mechanical damping of a rotor blade exceeds this critical level, any small bending motion imparted to the blade will decay in time. Hence the system is stable and flutter will not occur. However, if δ_{Onset} is greater than the available mechani-

cal damping of a rotor blade, any small bending motion imparted to the blade will cause the blade to flutter.

In the next section the present analysis is used to predict the flutter boundaries of four high-speed fan rotors. The results are compared with the measured flutter boundaries to establish the validity of the analysis.

RESULTS

For the flutter mode under study the amplitude of the motion increases monotonically along the blade span from the node line. For blades that are rigidly fixed at their root (i.e., mechanically constrained), the node line can be assumed to lie outboard of the blade platform (i.e., outboard of the aerodynamic hub of the blade). The node line of the first flexural mode of the rotors to be investigated later in this section is approximately 20 percent of span height outboard of the platform. Thus, the vibratory motion of the blades in these rotors at any spanwise section is

$$h_1 = -\xi \sin \overline{\theta}'^{(20\%)} \tag{114}$$

$$h_2 = \xi \cos \overline{\theta}'^{(20\%)} \tag{115}$$

where ξ is the amplitude of the motion at the section and $\overline{\theta}'^{(20\%)}$ is the stagger angle at 20 percent of span.

The aerodynamic work per unit of span at a given radial location depends on the amplitude of the motion of the section and the relative dynamic pressure of the incoming streamline to the section. Thus because both increase with distance from the hub, the total work done by the airstream on a blade is strongly influenced by the unsteady flow field surrounding the tip region. A simple calculation shows that this influence encompasses the outer 25 percent of the span. If the outer-casing boundary layer were assumed to influence the flow field over 5 percent of the tip region of a blade, a direct correlation might exist between the flutter boundary of a rotor and a two-dimensional cascade whose geometry and dynamic response coincide with that of the rotor at 85 percent of span (i.e., algebraic means of 75 and 95 percent of span). The results presented in the remainder of this section are based on this premise.

The objective of the first series of calculations is to establish the influence of reduced frequency k_b and interblade phase angle on the aeroelastic stability of a cascade of airfoils. For this study a normalized damping parameter defined as

$$\delta_N = -\frac{1}{2}\frac{\overline{\rho}_{-\infty}}{\overline{\rho}_{0,\mathrm{Amb}}}\frac{1}{k_b^2}\frac{\pi}{\tilde{\xi}}\left[-\sin\overline{\theta}'(20\%)\,\mathcal{I}m\left(\tilde{F}_1\, e^{-ik_2X_2}\, e^{-ikt}\right)\right.$$

$$\left. + \cos\overline{\theta}'(20\%)\,\mathcal{I}m\left(\tilde{F}_2\, e^{-ik_2X_2}\, e^{-ikt}\right)\right] \qquad (116)$$

is calculated as a function of k_b and the interblade phase angle. The parameter $\rho_{0,\mathrm{Amb}}$ in this equation is the inlet stagnation density measured in the absolute coordinate system. For δ_N greater than zero the airstream is supplying energy to the cascade. If the mechanical damping of the cascade system is zero, the operating condition would be unstable. For values of δ_N less than zero the cascade is doing work on the airstream, and hence the system is stable.

Solving equation (116) requires as input information the steady-state inlet flow properties, the geometry of the cascade, and the frequency of oscillation. A set of loss and deviation-angle correlations must also be specified. The present analysis makes use of the correlations derived in appendix C. The steady-state inlet flow conditions are derived from the blade-element data, measured at 85 percent of design speed, of the second stage of the NASA 1450-ft/sec-tip-speed two-stage fan. (This rotor is analyzed in greater detail later in this section. This blade-element data set is reported in reference 6. The cascade geometry represents the geometry of the second-stage rotor element at 85 percent of span height from the hub.

Figure 5 shows a plot of δ_N as a function of interblade phase angle and reduced frequency k_b for the NASA fan operating at the flutter boundary at 85 percent of design speed. This figure shows that the bending flutter mode is associated with a positive interblade phase angle (i.e., implies that the vibration pattern is traveling around the rotor in the direction of rotation). The figure also shows that increasing the reduced frequency stabilizes the motion at a constant interblade phase angle.

Figure 6 shows a plot of δ_N as a function of interblade phase angle and percentage of design weight flow along the 85-percent-speed line. For a given interblade phase angle, decreasing the weight flow at constant wheel speed (i.e., increasing the steady-state aerodynamic loading) tends to destabilize the rotor.

From the results shown in figures 5 and 6 the present analysis seems to predict that δ_N increases monotonically with interblade phase angle over the range shown. Hence, unless some additional information is supplied that establishes the interblade phase angle at the onset of flutter, the analysis in its present form cannot be used to predict supersonic stall bending flutter. In attempting to solve this

problem it was observed that the variable k_2 (and hence the interblade phase angle) appeared in several of the terms in the analysis (e.g., eq. (77)) as a result of expanding the quantity

$$N\left(e^{ik_2/N} - 1\right) \tag{117}$$

to first order in k_2/N. It might therefore be expected that replacing k_2 in the analysis with the imaginary part of $N\left(e^{ik_2/N} - 1\right)$

$$\mathcal{I}m\left[N\left(e^{ik_2/N} - 1\right)\right] = N \sin\frac{k_2}{N} \tag{118}$$

would give a more physically realistic behavior for large values of k_2. This modification was introduced into all the expressions containing k_2 except the exponential factor $e^{ik_2X_2}$. The results obtained from this altered analysis are shown in figure 7. For $|\sigma| \leq 45^\circ$, the modified analysis yields results that are comparable to those obtained from the original formulation. In addition the modified analysis predicts a finite maximum for δ_N.

The validity of the modified analysis as a correlation system for predicting the onset of supersonic stall bending flutter can be established by showing that, for a given rotor, flutter will generally be observed whenever the predicted maximum value of δ_N exceeds the normalized structural damping of the rotor. For this demonstration, four high-speed fan stages were investigated. The level of structural (i.e., log decrement) damping (assumed to be a constant for each rotor) to be used in this study had to be estimated from experimental flutter data. The first rotor to be analyzed in this study is the second stage of the NASA 1450-ft/sec two-stage fan. The performance map for this fan is shown in figure 8. The second stage exhibits two zones of bending flutter, both of which are shown in figure 8. The first flutter zone occurs at part speed and lies close to the fan stall line. The second zone occurs at operating speeds in excess of design speed. Because this second flutter zone appears to be associated with a choked passage flow, it will not be analyzed in this study.

The maximum value of the normalized aerodynamic damping δ_N (denoted herein by the symbol $\delta_{N,max}$) as a function of weight flow and wheel speed for the second-stage fan is shown in figure 9. The operating point at 85 percent of design speed at which flutter occurred is denoted by the solid symbol. (Open symbols denote stable operating conditions.) If the level of mechanical damping in the system were equal to the aerody-

namic damping at this operating point, the altered analysis would predict that all the remaining operating points are stable, including the stall points at 75 and 95 percent of design speed. This result is supported by experimental results. An attempt was made to shift the flutter boundaries of this fan out of its stable operating range by closing the first-stage stator blades. This reduced the magnitude of the relative velocity entering the second stage and increased the relative incidence angle to the stage. Reducing the velocity raised the reduced frequency and, from previous results, is a stabilizing factor. However, increasing the incidence angle increased the aerodynamic loading on the rotor and from previous calculations, is a destabilizing factor.

The computed results for $\delta_{N,max}$ at the two operating points (80 and 85 percent of design wheel speed) at which blade-element aerodynamic data were recorded are shown in figure 10. For a value of mechanical damping estimated from the results presented in figure 9, the analysis predicts that the modified design would experience bending flutter at these two operating points. Figure 11 shows the predicted flutter boundary for the modified fan superimposed on its performance map. The experimental flutter boundary is also indicated in this figure. Comparing the results presented in figure 11 with those presented in figure 9 shows that the analysis predicts a shift in the flutter boundary of the second stage as a result of the configuration change. The predicted shift of the boundary is consistent with the experimental data; however, the extent of the flutter region is overestimated by the correlation.

The present analysis can be used to study the effect of the steady, inviscid aerodynamic force on the supersonic stall flutter boundary. For example, reference 9 has shown that at low speeds the steady, inviscid aerodynamic force can induce bending flutter. In the present study, the aerodynamic damping was calculated as a function of interblade phase angle, and the effect of loss and deviation-angle variations was neglected. This calculation was performed with, as input data, the rotor geometry and the aerodynamic inlet conditions at the predicted flutter point of the NASA two-stage fan. The results of this calculation are shown in figure 12, along with the results from figure 7, which include the effects of the viscous forces. (The range over which the results were calculated was chosen to be of sufficient width to include the interblade phase angles measured at the onset of flutter reported in ref. 8.) This figure clearly shows that the steady, inviscid forces in themselves are not the primary destabilizing force at high speeds. Rather it appears that supersonic stall bending flutter is induced by the viscous forces associated with a rapid rise in the tip blade-element loss coefficient.

The present analysis was also correlated and verified with the flutter data obtained from fan C of the NASA Quiet Engine Program (ref. 6), the NASA 50-50 fan stage, and a prototype fan rotor developed in industry. The performance map for fan C (fig. 13) shows two flutter instability zones. The first zone is torsional flutter that occurs at part speed and lies close to the stall line. Just above this zone lies a zone of bending

flutter that appears to extend past 95 percent of design speed. Only the bending flutter mode of this rotor is analyzed in this report. The maximum value of the calculated, normalized damping as a function of weight flow and wheel speed for fan C is shown in figure 14. The operating points at which flutter occurred are indicated by the solid symbols. (Open symbols denote measured stable operating conditions.) The level of mechanical damping for this rotor system is assumed to equal the minimum value of the aerodynamic damping computed at the operating point where flutter was encountered. This level of damping was used to calculate the stability boundary in figure 14. All operating points that lie above this boundary are assumed to be unstable, and those that lie below are assumed to be stable. The majority of the measured stable operating points lie below the estimated stability boundary. The results of transforming this boundary onto the performance map is shown in figure 15. The solid symbols in this figure denote measured flutter points. This figure shows that the present model yields results that are consistent with measured experimental data.

The rotor of the NASA 50-50 fan stage encountered supersonic bending flutter at 100 percent of design wheel speed at reduced inlet pressure (1/2 atm). At standard inlet conditions (1 atm) the flutter zone intersected the stall boundary at 90 percent of design wheel speed. Both boundaries are shown on the rotor performance map of figure 16. The magnitude of the maximum normalized damping along the 100- and 90-percent-speed lines for this rotor is shown in figure 17. The experimental flutter point at reduced inlet conditions is indicated in the figure by the solid symbol. This point is assumed to define the mechanical damping level of the rotor system. Figure 17 shows that the analysis predicts that all the stable operating points at reduced inlet conditions lie below the stability boundary.

For a constant inlet-total-temperature operating condition the present analysis predicts that the aerodynamic damping acting on the NASA 50-50 fan stage will increase linearly with inlet total pressure. Thus if the mechanical damping of this rotor system were independent of the inlet total pressure, the predicted flutter zone on the performance map of this fan would increase as the inlet pressure was raised. In figure 18 the predicted flutter boundary for the NASA 50-50 fan stage at an inlet pressure of 1 atmosphere is superimposed on its performance map. Also shown in this figure is the measured flutter boundary at that inlet pressure. Comparing these two sets of results with the measured flutter boundary at 1/2-atmosphere inlet pressure shown in figure 16 suggests that the present analysis overestimates the destabilizing influence of higher inlet pressure on this fan stage.

A prototype fan rotor developed in industry was also run at two levels of inlet pressure. The flutter boundaries for this fan are shown on its performance map in figure 19. The maximum normalized damping for this fan is shown as a function of weight flow and wheel speed in figure 20. The experimental flutter point for this fan

is denoted by the solid symbol. This point is used to define the stability boundary at atmospheric inlet conditions. Once again, the analysis predicts that all the measured stable operating points of this fan lie below this boundary.

For a level of mechanical damping in the rotor system estimated from the results shown in figure 20, the analysis was used to establish the flutter boundary at a raised inlet pressure of 2 atmospheres. The predicted boundary and the measured flutter boundary at this higher pressure are shown on the performance map in figure 21. The measured flutter boundary intersects the stall line at 81 percent of design wheel speed; the predicted flutter boundary intersects the stall line at 71 percent of design wheel speed. As in the previous study, the analysis slightly overestimated the destabilizing influence of raised inlet pressure on the flutter boundary of a fan stage.

The present analysis has been used with good success to predict the bending flutter boundaries of four transonic compressor rotors. These boundaries were calculated from empirically derived estimates for the mechanical damping level in each rotor. The material damping level (i.e., log decrement) of a compressor rotor blade was reported in reference 4 to lie between 0.008 and 0.02. For the NASA two-stage fan the estimated damping level of 0.0125 lies within the material damping range reported in reference 4. This was expected since this rotor was designed for rig testing and thus was of fairly rigid and massive construction. For the remaining rotors the estimated levels of damping used in calculating their flutter boundaries were 0.0246 for fan C, 0.0298 for the NASA 50-50 fan stage, and 0.0218 for the prototype fan stage. These levels of damping are greater than the level of material damping reported in reference 4. The greater overall damping levels in these rotors are attributed to their greater flexibility (i.e., these rotors were assembled from engine flight hardware). This flexibility could allow the various components of the rotor assembly to rub against one another during a cycle of motion. This rubbing motion would result in friction damping, which - added to the material damping of these rotors - would yield a total damping level greater than that in comparable rig rotor assemblies. Thus in using the present analysis as a correlation for predicting the onset of supersonic stall bending flutter of a compressor stage, a damping level of about 0.0125 should be used if the rotor assembly is fairly rigid. However, if the rotor assembly is fairly flexible, such that during a flutter cycle the components of the assembly might be in relative motion, a damping level of about 0.025 should be assumed.

CONCLUDING REMARKS

In the present investigation an analytical model was developed to predict the onset of supersonic stall bending flutter in high-speed rotors. This model was based on the

assumption that there is a direct correlation between the onset of bending flutter in a rotor and the onset of bending flutter in a two-dimensional cascade whose geometry, dynamic response, and aerodynamic performance coincide with the rotor blade-element section at 85 percent of span height measured from the hub. The two-dimensional cascade of airfoils was considered as an actuator disk that was allowed to deform in time. The effects of shock waves and viscous forces were introduced into the model through rotor blade-element total-pressure-loss and deviation-angle correlations. The information input to the analysis is the steady aerodynamic inlet flow conditions to the rotor blade-element section at 85 percent of span height, the rotor geometry, and the rotor's dynamic response. In addition, aerodynamic design information must be specified, along with a value for the structural damping in the rotor assembly.

To verify the analysis, computed flutter boundaries of four high-speed fan stages that experienced supersonic stall flutter were compared with their measured boundaries. These four rotors covered a range of design parameters typical of present and advanced fan designs. For this verification study the structural damping level had to be deduced from the experimental flutter data.

The stability boundaries predicted by the analysis were in good agreement with the experimental results. Any difference that did exist showed the analysis to slightly overestimate the extent of the flutter region. Although no specific reason for this apparent conservatism is obvious, several possible reasons are (1) the assumed structural damping model, (2) the use of rotor blade-element quasi-steady loss and deviation-angle correlations, (3) three-dimensional aeroelastic effects, and (4) the assumed form for the interblade-phase-angle dependency used in the model. Finally the validation studies clearly showed that the primary destabilizing forces in supersonic stall bending flutter are the viscous forces associated with a rapid rise in the tip blade-element, total-pressure-loss coefficient.

Additional experimental data are needed to improve the present correlation between the measured and predicted flutter boundaries of a fan stage and to broaden the general applicability of the model. In particular, experimental measurements are needed to establish the influence of rotor geometry, weight flow, and wheel speed on the flutter boundary and the interblade phase angle at the onset of flutter. In addition, a comprehensive analytical and experimental program is needed to establish the mechanism and level of structural damping in a rotor assembly.

Lewis Research Center,
National Aeronautics and Space Administration,
Cleveland, Ohio, August 9, 1978,
510-55.

APPENDIX A

SYMBOLS

b	airfoil semichord
C_p	specific heat at constant pressure
$C_{\pm\infty}$	complex constant
c	average blade chord and damping coefficient
d	circumferential distance around wheel
E	complex constant
F_i	aerodynamic force
h	enthalpy
h_1	axial displacement of an airfoil
h_2	tangential displacement of an airfoil
i	$\sqrt{-1}$
K	constant
k	reduced frequency based on circumferential distance, $\omega d/q_{-\infty}$
k_b	reduced frequency based on semichord, $\omega b/q_{-\infty}$
k_2	wave number of disturbance along cascade plane
M	Mach number
m	defined by eq. (C2)
m_b	mass of a rotor blade per unit length
N	number of blades in rotor
n	integer
n_i	unit vector
p	pressure
q	magnitude of velocity field
R	radial distance
RQ	defined by eq. (36)
R_i	complex constant
S	complex constant

s	entropy
T	temperature
T_0	total temperature
t	time
U_i	velocity components
U^R	rotational velocity
W_{Aero}	aerodynamic work per cycle of motion
W_D	energy dissipated per cycle of motion by mechanical damping
w	mass flow rate
X_i	spacial coordinates
α	incidence angle
$\alpha_{\pm\infty}$	complex wave number in axial direction
α_{ij}	complex constants
β	flow angle
γ	ratio of specific heats; axial wave number
δ	log decrement; deviation angle, eq. (37)
δ_{m_1}	metal angle at leading edge
δ_{m_2}	metal angle at trailing edge
ζ	vorticity
θ	stagger angle
ξ	amplitude of blade motion
ρ	density
σ	solidity
τ	cascade pitch or average thickness of a rotor blade
Φ	velocity potential
χ	total-pressure-loss coefficient
Ψ	vector potential
ω	frequency of oscillation

Subscript:

$\pm\infty$ upstream or downstream variable

Superscripts:

$\bar{(\ )}$ steady-state variable

$\tilde{(\ )}$ time-dependent variable

$*$ complex conjugate

Rel relative component

APPENDIX B

PERTURBATION COEFFICIENTS

$$\alpha_{11} = \alpha_{-\infty} - \overline{M}_{-\infty}^2 \overline{U}_{1,-\infty} \left(ik + \overline{U}_{1,-\infty} \alpha_{-\infty} + \overline{U}_{2,-\infty} ik_2 \right)$$

$$\alpha_{12} = \overline{\rho}_\infty \overline{M}_\infty^2 (RQ) \overline{U}_{1,\infty} \left(ik + \overline{U}_{1,\infty} \alpha_\infty + \overline{U}_{2,\infty} ik_2 \right) - \overline{\rho}_\infty \alpha_\infty$$

$$\alpha_{13} = -\frac{\overline{\rho}_\infty ik_2}{\gamma_\infty^2 + k_2^2}$$

$$\alpha_{14} = \overline{\rho}_\infty \overline{M}_\infty^2 (RQ) \overline{U}_\infty (\gamma - 1) \overline{T}_\infty$$

$$R_1 = h_1 \left(ik + \overline{U}_{2,-\infty} ik_2 - \overline{\rho}_\infty ik - \overline{\rho}_\infty \overline{U}_{2,\infty} ik_2 \right)$$

$$\alpha_{21} = -k_2 k$$

$$\alpha_{22} = k_2 k$$

$$\alpha_{23} = \frac{\gamma_\infty k}{\gamma_\infty^2 + k_2^2} - \overline{U}_{1,\infty}$$

$$\alpha_{24} = \overline{T}_\infty ik_2$$

$$R_2 = kk_2 \left[\left(\overline{U}_{1,-\infty} - \overline{U}_{1,\infty} \right) h_1 + \left(\overline{U}_{2,-\infty} - \overline{U}_{2,\infty} \right) h_2 \right]$$

$$\alpha_{31} = -\sec^2 \overline{\beta}_\infty \left\{ \frac{\partial g}{\partial \beta_{-\infty}} \left(\overline{U}_{1,-\infty} ik_2 - \overline{U}_{2,-\infty} \alpha_{-\infty} \right) + \frac{\partial g}{\partial M_{-\infty}} \left[\overline{M}_{-\infty} \overline{U}_{1,-\infty} \alpha_{-\infty} + \overline{M}_{-\infty} \overline{U}_{2,-\infty} ik_2 \right. \right.$$

$$\left. \left. + \overline{M}_{-\infty}^3 \frac{\gamma - 1}{2} \left(ik + \overline{U}_{1,-\infty} \alpha_{-\infty} + \overline{U}_{2,-\infty} ik_2 \right) \right] \right\}$$

$$\alpha_{32} = \frac{ik_2}{\overline{U}_{1,\infty}} - \frac{\overline{U}_{2,\infty}\,\alpha_\infty}{\overline{U}^2_{1,\infty}}$$

$$\alpha_{33} = \frac{i\gamma_\infty}{\overline{U}_{1,\infty}\left(\gamma^2_\infty + k^2_2\right)} - \frac{\overline{U}_{2,\infty}}{U^2_{1,\infty}}\,\frac{ik_2}{\gamma^2_\infty + k^2_2}$$

$$\alpha_{34} = 0$$

$$R_3 = h_2\left(\frac{ik}{\overline{U}_{1,\infty}} - \sec^2\overline{\beta}_\infty\,\frac{\partial g}{\partial\beta_{-\infty}}\,ik\overline{U}_{1,-\infty} - \sec^2\overline{\beta}_\infty\,\frac{\partial g}{\partial M_{-\infty}}\,\overline{U}_{2,-\infty}\overline{M}_{-\infty}ik - \sec^2\overline{\beta}_\infty\,\frac{\partial g}{\partial\sigma}\,ik_2\overline{\sigma}\right)$$

$$+ h_1\left[-\frac{\overline{U}_{2,\infty}}{\overline{U}^2_\infty}\,ik + \sec^2\overline{\beta}_\infty\,\frac{\partial g}{\partial\beta_{-\infty}}\,\overline{U}_{2,-\infty}ik - \sec^2\overline{\beta}_\infty\,\frac{\partial g}{\partial M_{-\infty}}\,\overline{M}_{-\infty}\overline{U}_{1,-\infty}ik + \sec^2\overline{\beta}_\infty\,\frac{\partial g}{\partial\left(\frac{\partial h_1}{\partial X_2}\right)}\,ik_2\right]$$

$$\alpha_{41} = \frac{e}{2\gamma\overline{M}_{-\infty}}\,\frac{\overline{s}\gamma\overline{M}_{-\infty}}{\overline{p}_{0,-\infty}}\,\frac{\overline{\chi}}{\overline{p}_{0,-\infty}}\left\{(1-\gamma)M^2_{-\infty}\left(ik + \overline{U}_{1,-\infty}\,\alpha_{-\infty} + \overline{U}_{2,-\infty}ik_2\right) - 2\overline{U}_{1,-\infty}\,\alpha_{-\infty} + 2\overline{U}_{2,-\infty}ik_2\right.$$

$$- \frac{\partial \ln\chi}{\partial\beta_{-\infty}}\left(ik_2\overline{U}_{1,-\infty} - \overline{U}_{2,-\infty}\,\alpha_{-\infty}\right) - \frac{\partial \ln\chi}{\partial M_{-\infty}}\left[\overline{M}_{-\infty}\overline{U}_{1,-\infty}\,\alpha_{-\infty}\right.$$

$$\left.\left. + \overline{M}_{-\infty}\overline{U}_{2,-\infty}ik_2 + \overline{M}^3_{-\infty}\,\frac{\gamma-1}{2}\left(ik + \overline{U}_{1,-\infty}\,\alpha_{-\infty} + \overline{U}_{2,-\infty}ik_2\right)\right]\right\}$$

$$\alpha_{42} = 0$$

$$\alpha_{43} = 0$$

$$\alpha_{44} = 0$$

$$R_4 = -\frac{e^{s\gamma\overline{M}_{-\infty}}}{2\gamma\overline{M}_{-\infty}} \frac{\overline{\chi}}{\overline{p}_{0,-\infty}} \left\{ h_1 \left[2ik\overline{U}_{1,-\infty} - \frac{\partial \ln \chi}{\partial \beta_{-\infty}} \overline{U}_{2,-\infty} ik + \frac{\partial \ln \chi}{\partial M_{-\infty}} \overline{M}_{-\infty} \overline{U}_{-\infty} ik - \frac{\partial \ln \chi}{\partial \left(\frac{\partial h_1}{\partial X_2} \right)} ik_2 \right] \right.$$

$$\left. + h_2 \left[-2\overline{U}_{2,-\infty} ik + \frac{\partial \ln \chi}{\partial \beta_{-\infty}} ik\overline{U}_{1,-\infty} + \frac{\partial \ln \chi}{\partial M_{-\infty}} \overline{U}_{2,-\infty} \overline{M}_{-\infty} ik + \frac{\partial \chi}{\partial \sigma} \overline{\sigma} ik_2 \right] \right\}$$

APPENDIX C

TOTAL-TEMPERATURE RISE ACROSS A DEFORMING ACTUATOR DISK

In this appendix an equation is derived that relates the total-temperature rise across the deforming actuator disk to the upstream potential field and the downstream potential, vorticity, and entropy fields. The thermodynamic variables on each side of the disk satisfy the equation

$$T\,ds = dh - \frac{dP}{\rho} \tag{C1}$$

where h is the enthalpy of the gas stream. Since equation (C1) is a relation for the incremental change of state of the gas, it may also be written as

$$\frac{1}{\rho}\frac{\partial P}{\partial X_i} = \frac{\partial h}{\partial X_i} - T\frac{\partial s}{\partial X_i} \qquad i = 1,\ 2 \tag{C2}$$

Introducing equation (C2) into Euler's equation of motion

$$\frac{\partial U_i}{\partial t} + U_j\frac{\partial U_i}{\partial X_j} = -\frac{1}{\rho}\frac{\partial P}{\partial X_i} \tag{C3}$$

yields

$$\frac{\partial U_i}{\partial t} + U_j\frac{\partial U_i}{\partial X_j} = -\frac{\partial h}{\partial X_i} + T\frac{\partial s}{\partial X_i} \qquad i = 1,\ 2 \tag{C4}$$

Substituting the relation

$$U_j\frac{\partial U_i}{\partial X_j} = \frac{\partial}{\partial X_i}\left(\frac{U_jU_j}{2}\right) + U_j\left(\frac{\partial U_i}{\partial X_j} - \frac{\partial U_j}{\partial X_i}\right) \tag{C5}$$

into equation (B4) produces the result

$$\frac{\partial U_i}{\partial t} + U_j\left(\frac{\partial U_i}{\partial X_j} - \frac{\partial U_j}{\partial X_i}\right) = T\frac{\partial s}{\partial X_i} - \frac{\partial}{\partial X_i}\left(h + \frac{U_jU_j}{2}\right) \tag{C6}$$

For an ideal gas

$$h + \frac{U_j U_j}{2} = C_p T_0 \tag{C7}$$

where C_p is the specific heat of the gas at constant pressure and T_0 is the total temperature. Introducing equation (C7) into equation (C6) yields

$$\frac{\partial U_i}{\partial t} + U_j \left(\frac{\partial U_i}{\partial X_j} - \frac{\partial U_j}{\partial X_i} \right) = T \frac{\partial s}{\partial X_i} - C_p \frac{\partial T_0}{\partial X_j} \tag{C8}$$

This equation is often referred to as the Crooco-Vazonyi equation. The X_2 component of equation (C8) for the flow field upstream of the actuator disk (in nondimensional form) reduces to

$$\frac{\partial U_{2,-\infty}}{\partial t} = - \frac{1}{\gamma - 1} \frac{1}{\overline{M}^2_{-\infty}} \frac{\partial T_{0,-\infty}}{\partial X_2} \tag{C9}$$

since

$$\frac{\partial U_{2,-\infty}}{\partial X_1} - \frac{\partial U_{1,-\infty}}{\partial X_2} \equiv 0 \tag{C10}$$

and

$$S_{-\infty} \equiv 0 \tag{C11}$$

Similarly the relation for the flow field downstream of the deforming disk (in nondimensional form) is

$$\frac{\partial U_{2,\infty}}{\partial t} + U_{1,\infty} \tilde{\zeta} = T_\infty \frac{\partial s_\infty}{\partial X_2} - \frac{1}{\gamma - 1} \frac{1}{\overline{M}^2_{-\infty}} \frac{\partial T_{0,\infty}}{\partial X_2} \tag{C12}$$

where

$$\tilde{\zeta} = \frac{\partial U_{2,\infty}}{\partial X_1} - \frac{\partial U_{1,\infty}}{\partial X_2} \tag{C13}$$

Thus the difference in total temperature across the disk is equal to

$$-\frac{1}{\gamma-1}\frac{1}{\overline{M}_{-\infty}^2}\frac{\partial}{\partial X_2}\left(T_{0,\infty}-T_{0,-\infty}\right)=\frac{\partial}{\partial t}\left(U_{2,\infty}-U_{2,-\infty}\right)+U_{1,\infty}\tilde{\xi}-T_{\infty}\left(\frac{\partial\tilde{s}_{\infty}}{\partial X_2}\right) \tag{C14}$$

which, when expanded to first order, becomes

$$\frac{1}{\gamma-1}\frac{1}{\overline{M}_{-\infty}^2}\frac{\partial}{\partial X_2}\left(\tilde{T}_{0,\infty}-\tilde{T}_{0,-\infty}\right)=-\frac{\partial}{\partial t}\left(\tilde{U}_{2,\infty}-\tilde{U}_{2,-\infty}\right)-\overline{U}_{1,\infty}\tilde{\xi}+\overline{T}_{\infty}\left(\frac{\partial\tilde{s}_{\infty}}{\partial X_i}\right) \tag{C15}$$

APPENDIX D

DEVIATION-ANGLE AND LOSS CORRELATION

The deviation-angle correlation applied in the present analysis is based on a modified Carter's rule

$$\delta = \delta_0 + \frac{m(\theta')\varphi}{\sqrt{\sigma}} + r(\alpha - \alpha_D, M_{-\infty}) \tag{D1}$$

where φ is the camber angle of the blade cross section in radians and α_D is the incidence angle at the design point in radians. The variable δ_0 is the reference deviation angle for zero camber. This variable is assumed here to be a constant and is equal to the difference between the deviation angle at the design point and the deviation angle calculated from Carter's rule. The remaining variable m for a circular-arc airfoil is plotted as a function of stagger angle in reference 12 (p. 211). This graph is well approximated by the expression

$$m = 0.216 + 0.05013\,\theta' + 0.08617\,\theta'^2 \tag{D2}$$

where θ' is expressed in radians.

In the neighborhood of the design point the deviation angle for a tip section of a fan rotor is generally observed to be independent of incidence angle and Mach number; thus

$$r\left(\alpha - \alpha_D, M_{-\infty}\right)_{\alpha=\alpha_D} = 0 \tag{D3}$$

$$\frac{\partial r}{\partial \alpha}\left(\alpha - \alpha_D, M_{-\infty}\right)_{\alpha=\alpha_D} = 0 \tag{D4}$$

$$\frac{\partial r}{\partial M_{-\infty}}\left(\alpha - \alpha_D, M_{-\infty}\right)_{\alpha=\alpha_D} = 0 \tag{D5}$$

In addition the rate of change of the deviation angle with incidence away from the design point is generally observed to increase as the Mach number is increased. Based on these observations the expression

$$r = \frac{4.86 + 11.0\left(M_{-\infty} - 1\right)}{4.45 - 7.0\left(M_{-\infty} - 1\right)} \left\{ \left(\alpha - \alpha_D\right)^2 \tan\left(\alpha_D + \theta\right) + \left[1 + 2\tan^2\left(\alpha_D + \theta\right)\right] \frac{\left(\alpha - \alpha_D\right)^2}{3} \right\} \tag{D6}$$

was derived from a number of high-speed fan stages tested at NASA Lewis. The data used in deriving this correlation were recorded at approximately 85 percent of span height (measured from the hub). The rotor-blade cross sections were multiple circular arcs designed for high-speed operation (tip Mach number, ~1.4). The tip solidity of these rotors varied from 1.3 to 1.7.

From equation (60) of the main text and the definition

$$\beta_{-\infty}^{D} \equiv \alpha_D + \theta + \delta_{m_1} \tag{D7}$$

the quantity $\alpha - \alpha_0$ can be shown to be

$$\alpha - \alpha_D = \beta_{-\infty} - \beta_{-\infty}^{D} \tag{D8}$$

Incorporating equation (D8) into equation (D6) and introducing the result, along with equation (D2), into equation (D1) yield the deviation-angle correlation used in this analysis.

The total-pressure-loss correlation is derived from a graph of experimental data presented in reference 11 (p. 248). This correlation is expressed as

$$f(D) = \frac{\chi\gamma M_{-\infty}^2}{4} \frac{\cos\beta'_{\infty}}{\sigma} \frac{1}{\left[\left(1 + \frac{\gamma - 1}{2} M_{-\infty}^2\right)^{\gamma/(\gamma-1)} - 1\right]} \tag{D10}$$

where D represents the flow diffusion through a blade passage. For a two-dimensional compressible flow, D is defined as

$$D = 1 + \frac{\cos\beta'_{-\infty}}{2\sigma} - \frac{M_{\infty}}{M_{-\infty}} \left(\frac{1 + \frac{\gamma - 1}{2} M_{-\infty}^2}{1 + \frac{\gamma - 1}{2} M_{\infty}^2} \right) \left(1 + \frac{\cos\beta'_{\infty}}{2\sigma} \right) \tag{D11}$$

An analytical expression for f(D) was derived by fitting a quadratic equation to the correlated experimental data of reference 11, measured at 85 percent of span height. The result is

$$f(D) = 0.03045 - 0.206\,D + 0.48175\,D^2 \tag{D12}$$

Introducing equations (D11) and (D12) into equation (D10) produces an expression for the loss coefficient χ in terms of inlet and exit flow angles, inlet and exit Mach numbers, and solidity. This expression, along with the deviation-angle correlation and the steady flow equations (eqs. (37), (44), (51), and (80)), forms a system of nonlinear algebraic equations whose solution yields the exit Mach number and exit flow angle as a function of inlet flow angle and Mach number, blade-section geometry, and design inlet and exit flow angles. From this solution the loss coefficient, as well as all the partial derivatives that appear in equations (73) and (86), can be calculated.

REFERENCES

1. Kurosaka, M.: On the Unsteady Supersonic Cascade with a Subsonic Leading Edge - An Exact First Order Theory: Parts 1 and 2. Transactions of the ASME: J. Eng. Power, vol. 96, no. 1, Jan. 1974, pp. 13-31.

2. Verdon, Joseph M.; and McCune, James E.: Unsteady Supersonic Cascade in Subsonic Axial Flow. AIAA J., vol. 13, no. 2, Feb. 1975, pp. 193-201.

3. Snyder, L. E.; and Commerford, G. L.: Supersonic Unstalled Flutter in Fan Rotors; Analytical and Experimental Results. J. Eng. Power, vol. 96, no. 4, Oct. 1974, pp. 379-386.

4. Goldstein, M. E.; Braun, W.; and Adamczyk, J. J.: Unsteady Flow in a Supersonic Cascade with Strong In-Passage Shocks. J. Fluid Mech., vol. 83, pt. 3, 1977, pp. 569-604.

5. Ruggeri, Robert S.; and Benser, William A.: Performance of a Highly Loaded Two-Stage Axial-Flow Fan. NASA TM X-3076, 1974.

6. Giffin, R. G.; Parker, D. E.; and Dunbar, L. W.: Experimental Quiet Engine Program Aerodynamic Performance of Fan C. (General Electric Co., NASA Contract NAS3-12430.) NASA CR-120981, 1972.

7. Loiseau, H.; and Maquennehan, B.: Aeroelastic Instabilities in Compressors and Tests in a Rectilinear Blade Cascade Wind Tunnel. Revue Francaise de Mecanique, Special Issue, 1976, pp. 157-167.

8. Whitehead, D. S.: Bending Flutter of Unstalled Cascade Blades at Finite Deflection. No. 3386, British A. R. C., 1965.

9. Whitehead, D. S.: The Vibration of Cascade Blades Treated by Actuator Disc Methods. Inst. Mech. Eng. (London), Proc., vol. 173, no. 20, 1959, pp. 555-563.

10. Lamb, H.: Hydrodynamics. Sixth Ed. Univ. Press (Cambridge), 1932.

11. Johnsen, I. A.; and Bullock, R. O.: Aerodynamic Design of Axial-Flow Compressors. NASA SP-36, 1965.

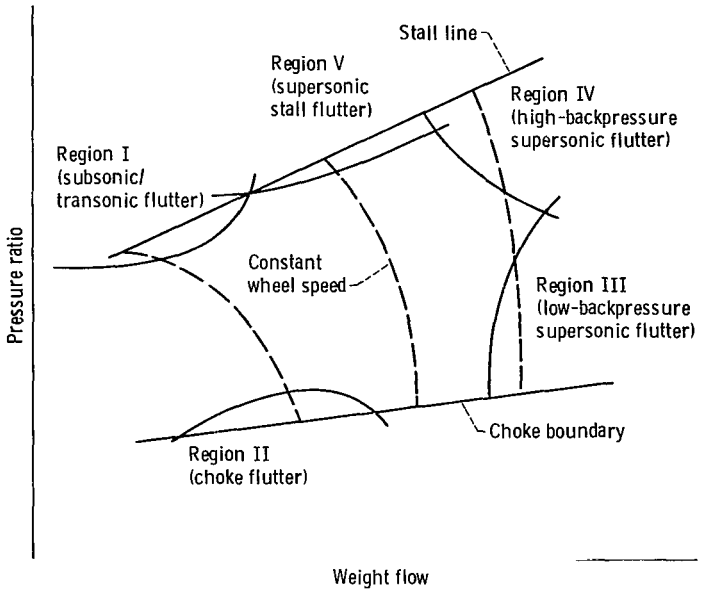

Figure 1. - Compressor performance and stability map.

Curve	Static pressure	
	kN/m^2	(psia)
1	82	(12)
2	89	(13)
3	96	(14)
4	103	(15)
5	110	(16)
6	117	(17)
7	124	(18)
8	131	(19)
9	137	(20)
10	144	(21)

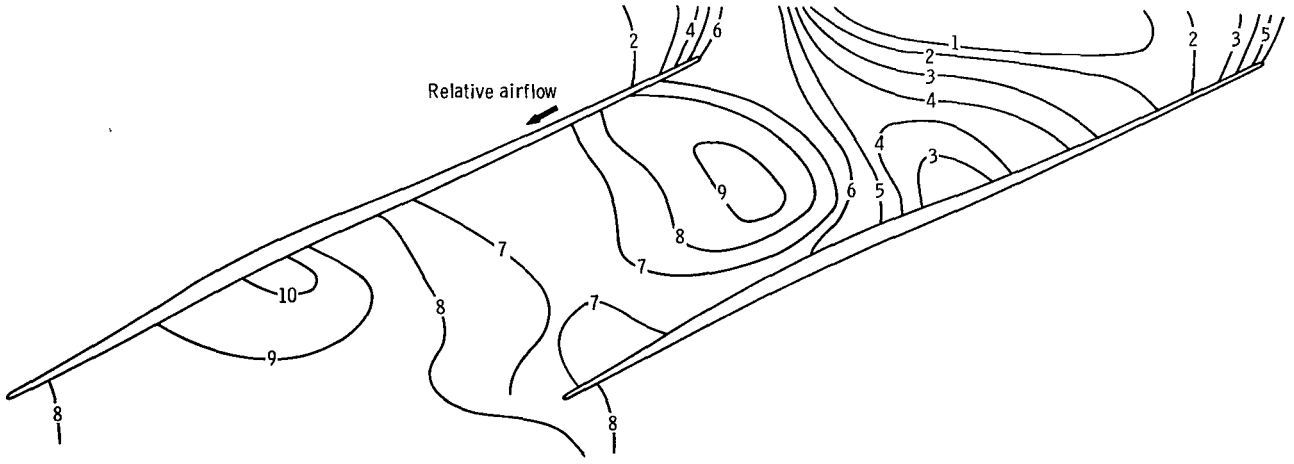

Figure 2. - Typical tip rotor static-pressure distribution near supersonic stall flutter boundary.

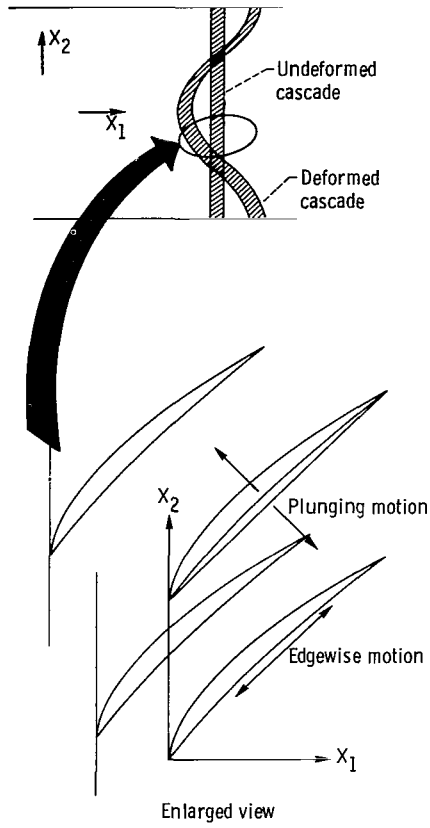

Figure 3. - Cascade plane deformation.

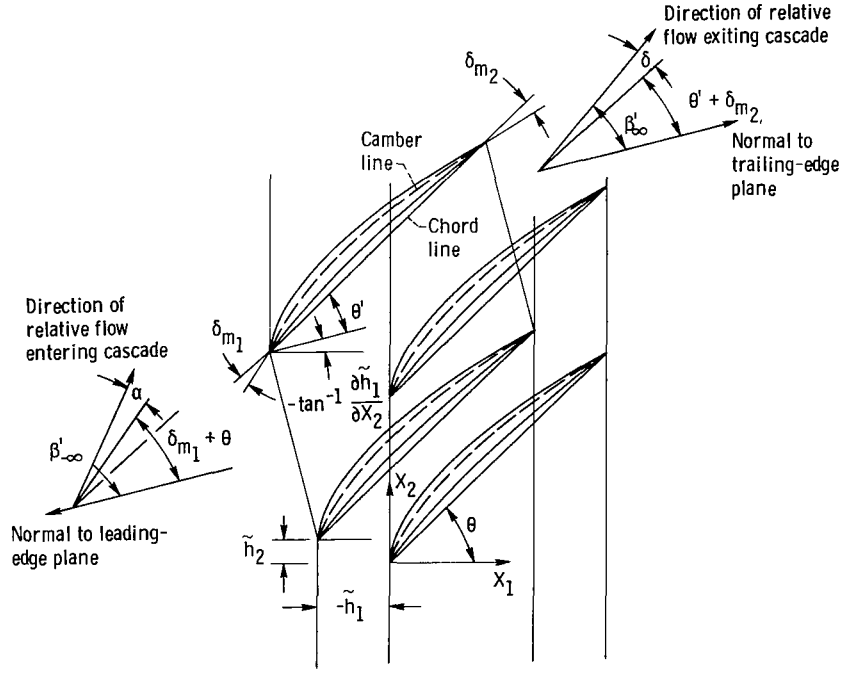

Figure 4. - Geometry of deformed cascade.

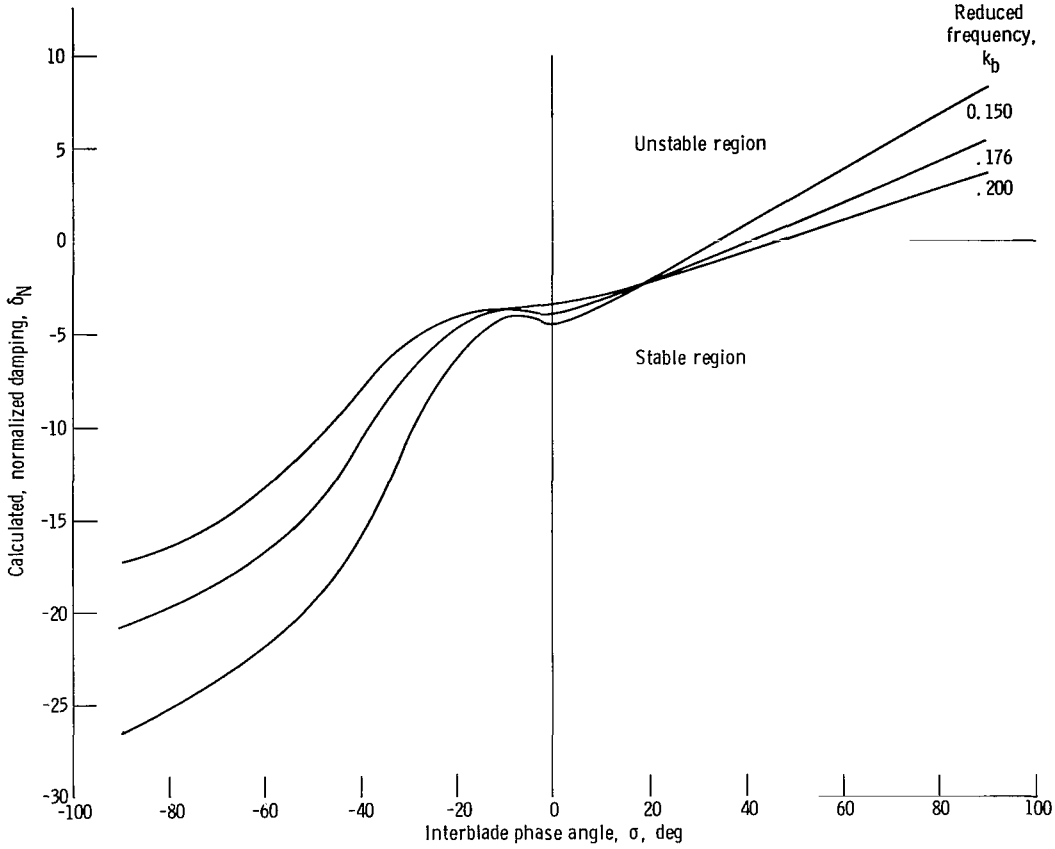

Figure 5. - Calculated, normalized damping as a function of interblade phase angle and reduced frequency for NASA two-stage fan.

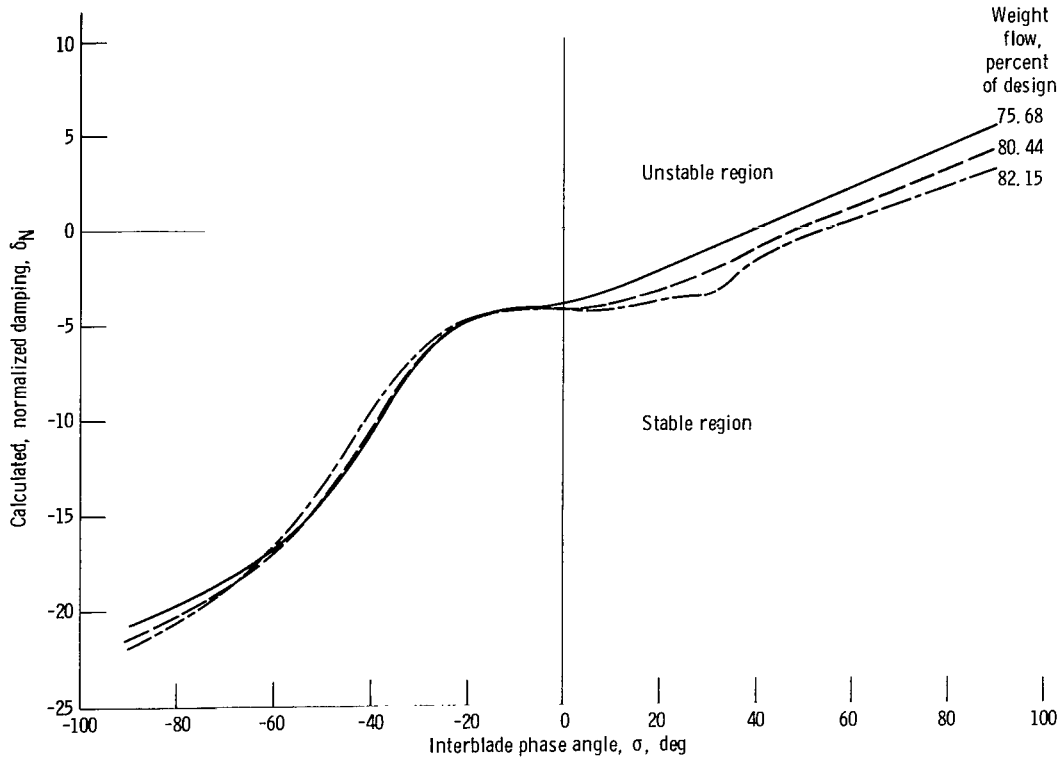

Figure 6. - Calculated, normalized damping as a function of interblade phase angle and weight flow for NASA two-stage fan at 85 percent of design wheel speed.

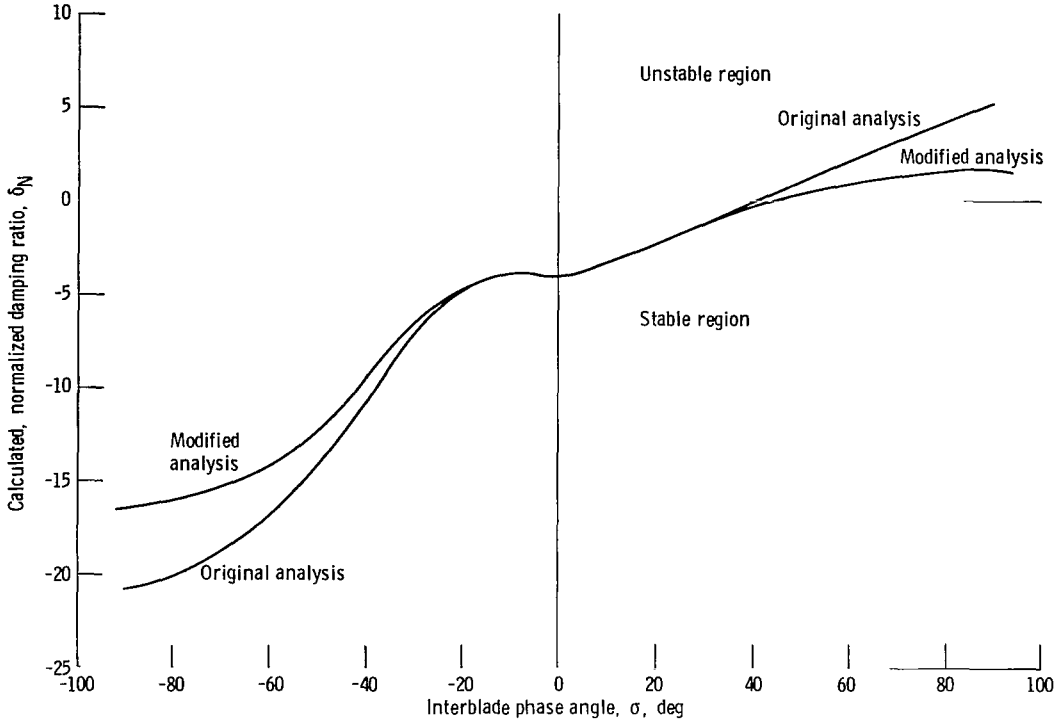

Figure 7. - Original and modified analyses for NASA two-stage fan at 85 percent of design wheel speed and 75.68 percent of design weight flow.

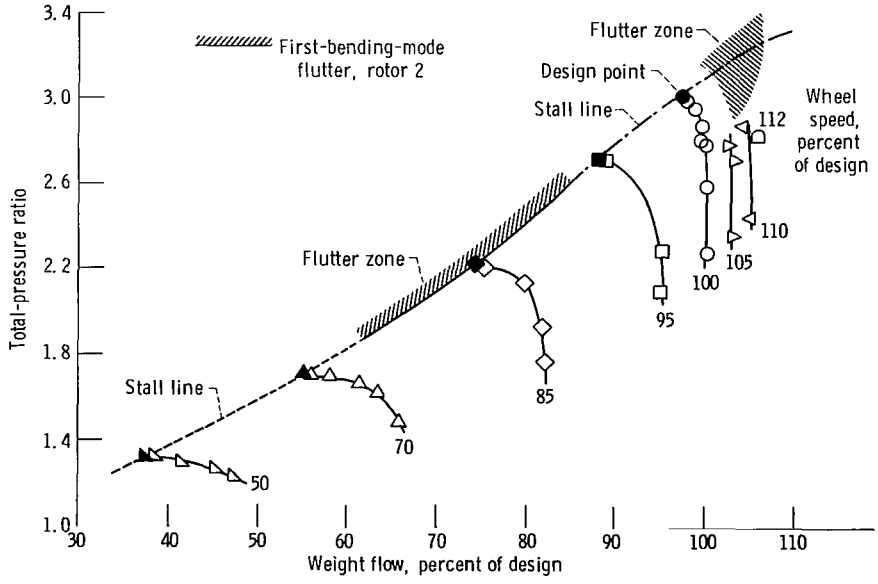

Figure 8. - Performance map for NASA two-stage fan.

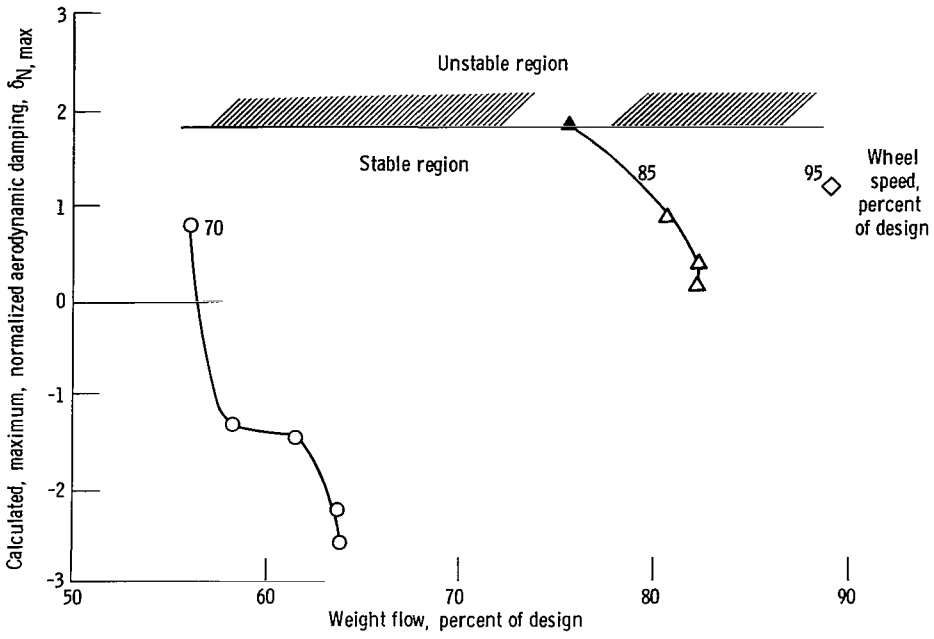

Figure 9. - Calculated, maximum, normalized aerodynamic damping as a function of weight flow and speed for NASA two-stage fan.

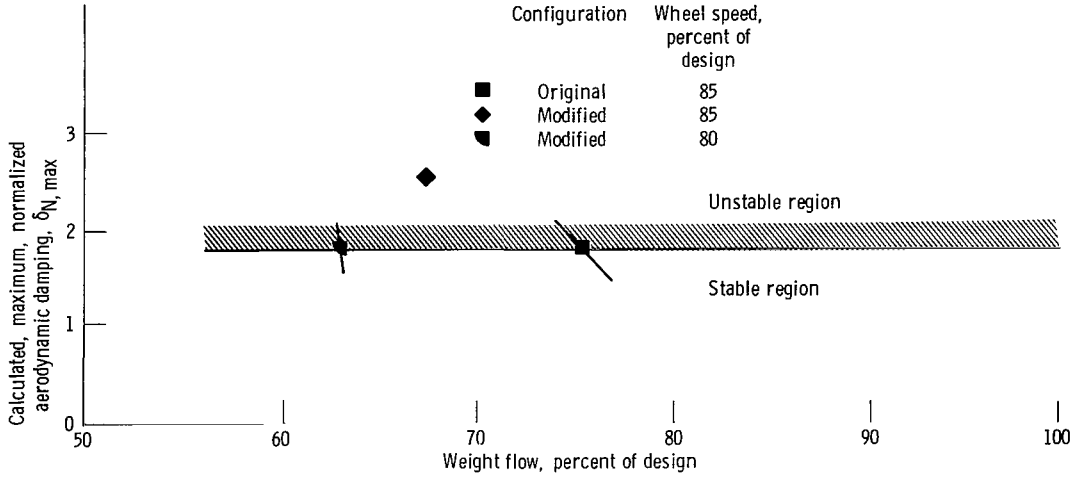

Figure 10. - Calculated, maximum, normalized aerodynamic damping as a function of configuration for modified NASA two-stage fan.

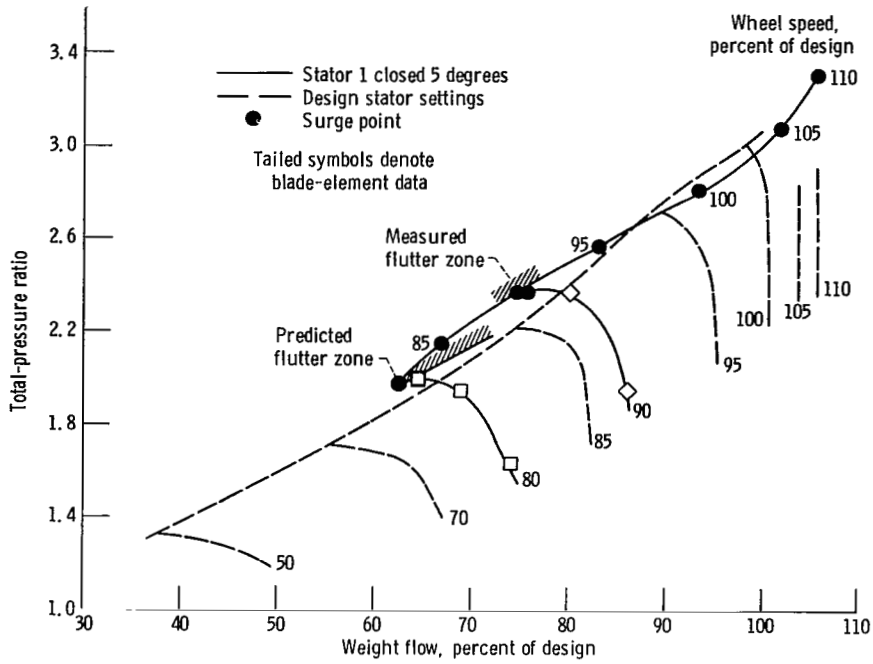

Figure 11. - Fan overall performance with first stator of NASA two-stage fan closed 5 degrees from design.

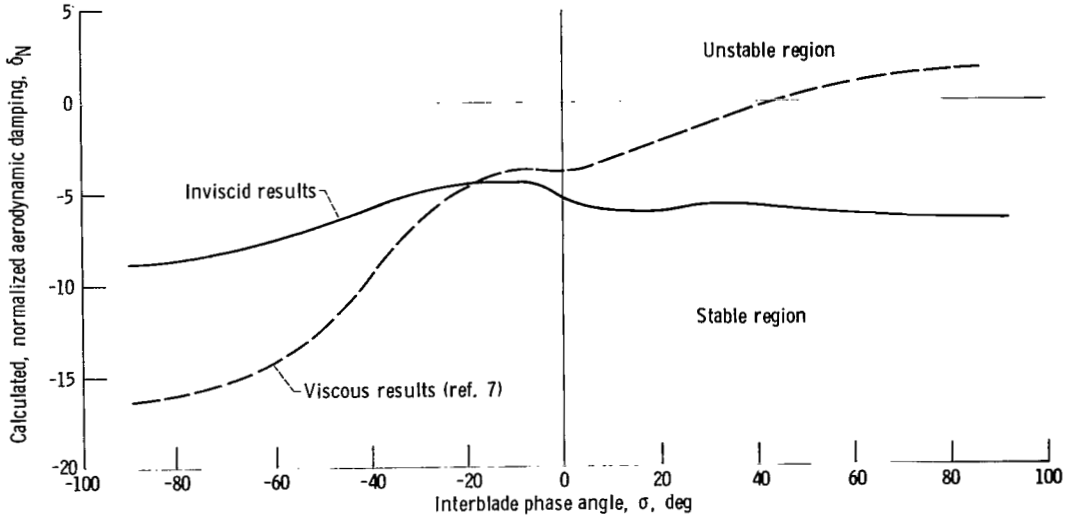

Figure 12. - Effect of viscous forces on normalized aerodynamic damping for NASA two-stage fan at 85 percent of design wheel speed and 75.68 percent of design weight flow.

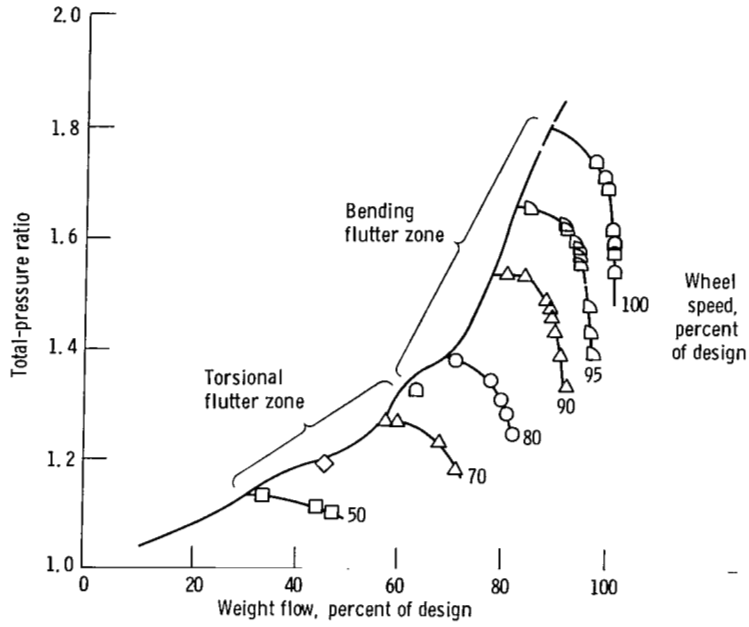

Figure 13. - Performance map for NASA Quiet Engine fan C.

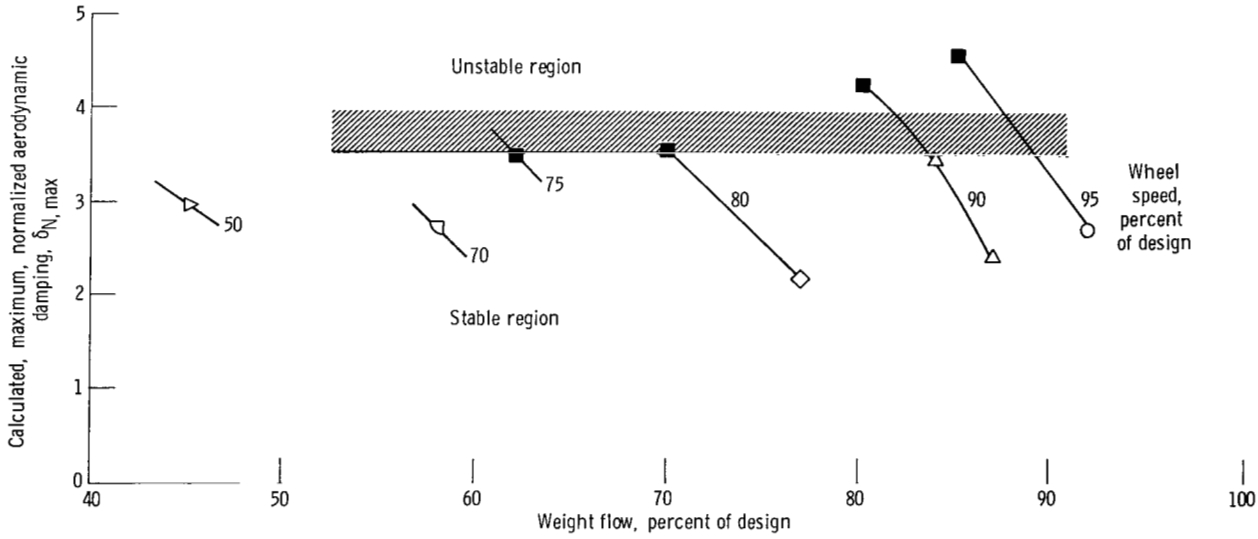

Figure 14. - Maximum normalized damping as a function of weight flow and wheel speed for fan C.

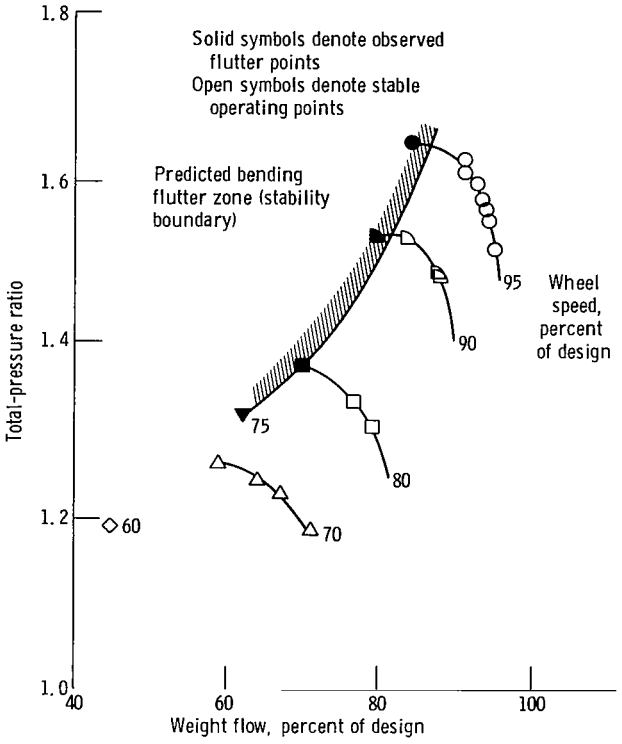

Figure 15. - Fan C performance map showing stability boundary from figure 14.

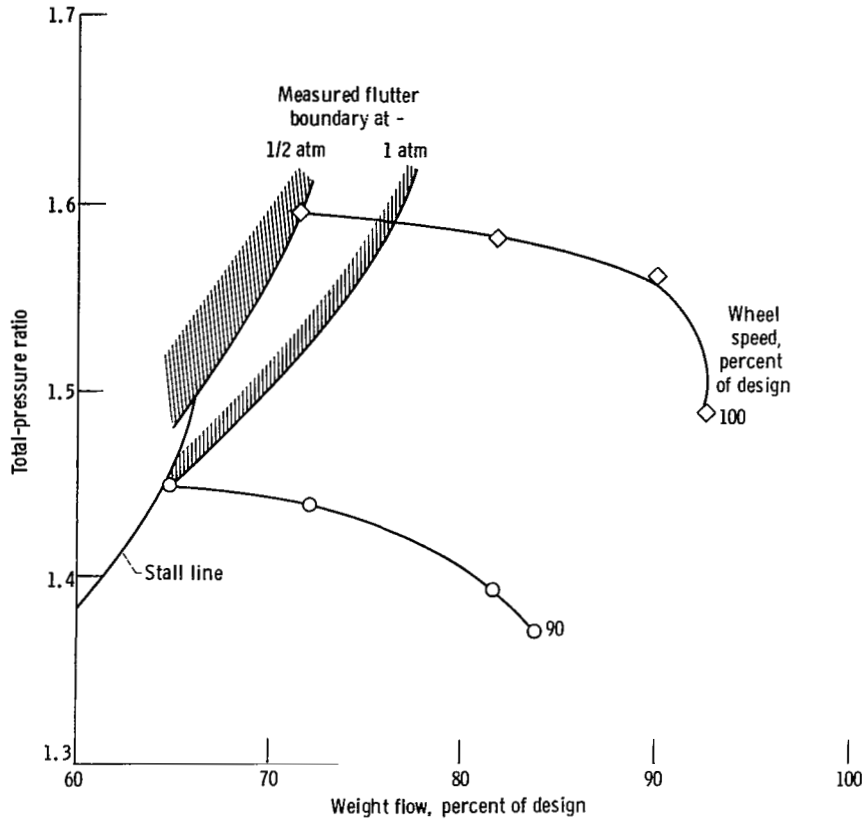

Figure 16. - Total-pressure ratio as a function of weight flow and wheel speed for NASA 50-50 fan stage.

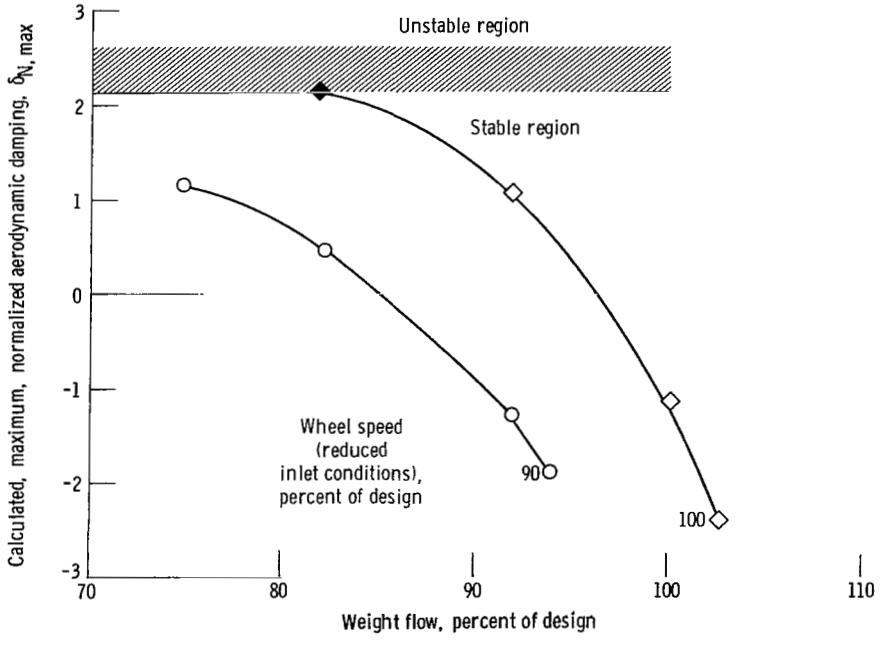

Figure 17. - Calculated, maximum, normalized aerodynamic damping at reduced inlet conditions as a function of weight flow and wheel speed for NASA 50-50 fan stage.

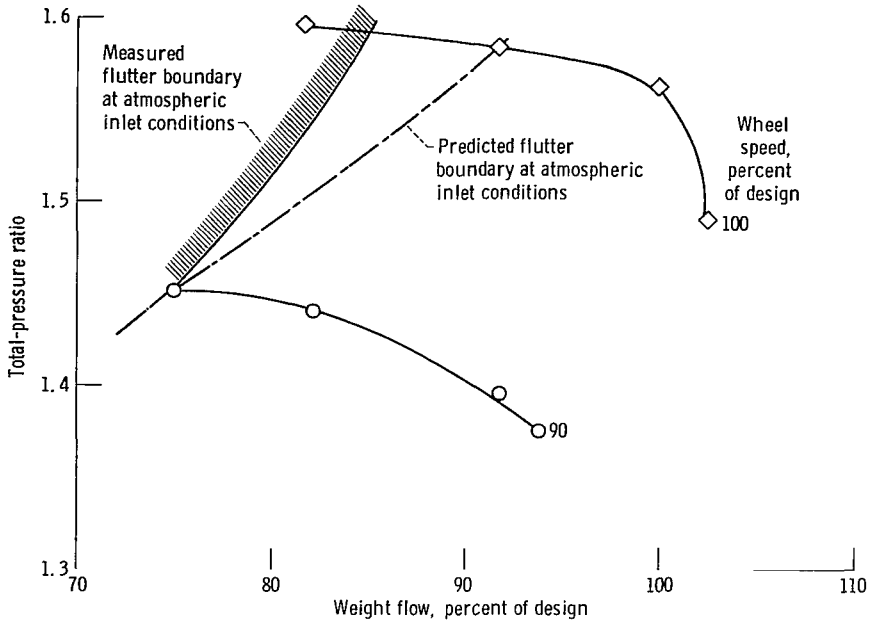

Figure 18. - Predicted bending flutter boundary at atmospheric inlet conditions for NASA 50-50 fan stage.

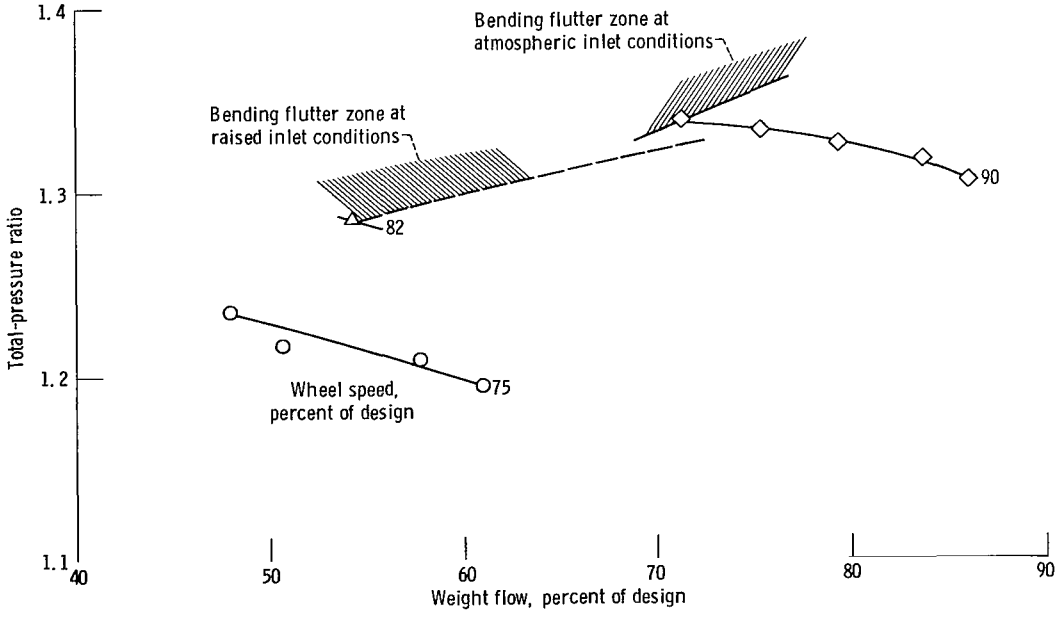

Figure 19. - Performance map for industrial fan stage.

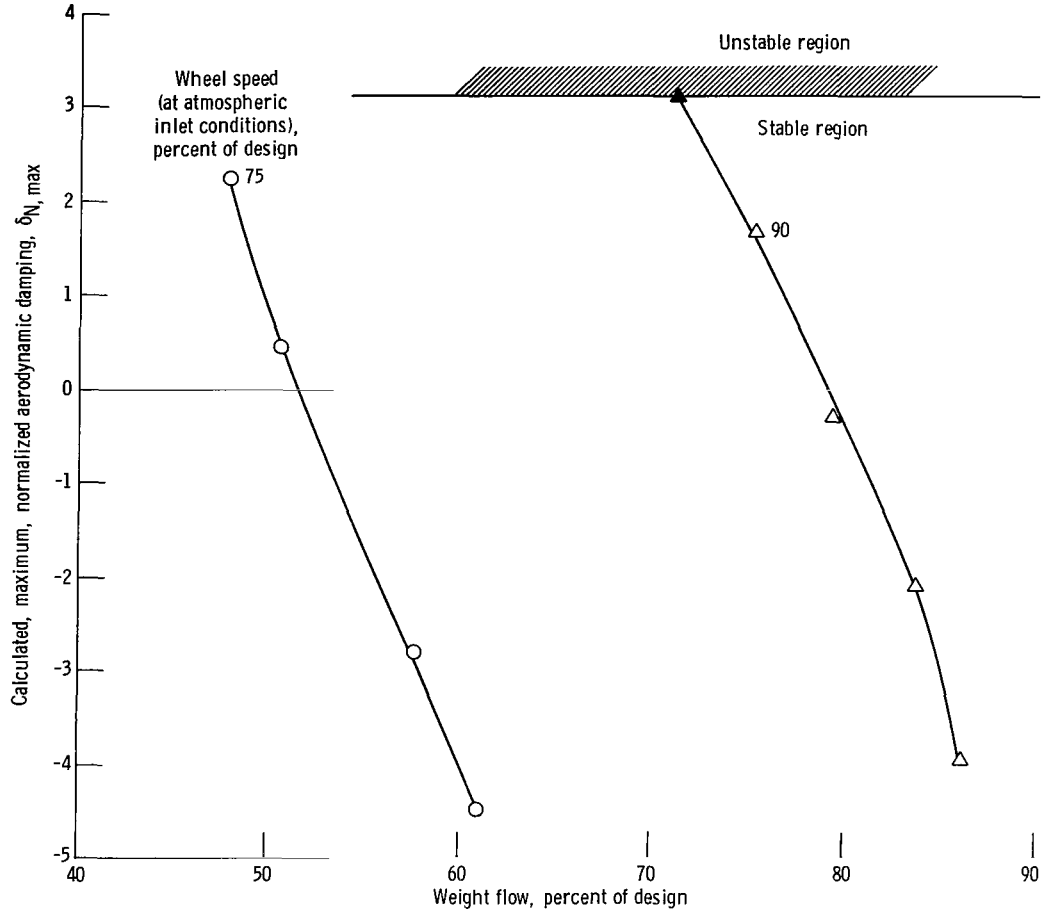

Figure 20. - Calculated, maximum, normalized aerodynamic damping as function of weight flow and wheel speed for industrial fan stage.

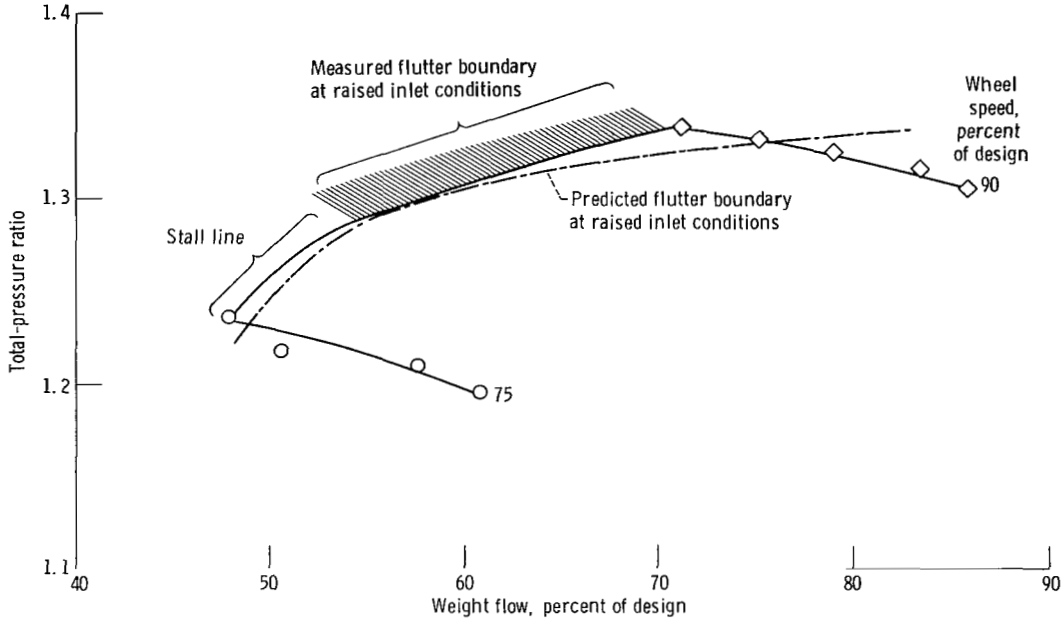

Figure 21. - Predicted bending flutter boundary at raised inlet conditions for prototype fan stage.

1. Report No.	2. Government Accession No.	3. Recipient's Catalog No.
NASA TP-1345		

4. Title and Subtitle
ANALYSIS OF SUPERSONIC STALL BENDING FLUTTER IN AXIAL-FLOW COMPRESSOR BY ACTUATOR DISK THEORY

5. Report Date
November 1978

6. Performing Organization Code

7. Author(s)
John J. Adamczyk

8. Performing Organization Report No.
E-9186

9. Performing Organization Name and Address
National Aeronautics and Space Administration
Lewis Research Center
Cleveland, Ohio 44135

10. Work Unit No.
510-55

11. Contract or Grant No.

12. Sponsoring Agency Name and Address
National Aeronautics and Space Administration
Washington, D.C. 20546

13. Type of Report and Period Covered
Technical Paper

14. Sponsoring Agency Code

15. Supplementary Notes

16. Abstract

An analytical model was developed for predicting the onset of supersonic stall bending flutter in axial-flow compressors. The analysis is based on two-dimensional, compressible, unsteady actuator disk theory. It is applied to a rotor blade row by considering a cascade of airfoils whose geometry and dynamic response coincide with those of a rotor blade element at 85 percent of the span height (measured from the hub). The effects of shock waves and flow separation are included in the model through rotor total-pressure-loss and deviation-angle correlations. Calculations show that the model predicts the onset, in an unshrouded rotor, of a bending flutter mode that exhibits many of the characteristics of supersonic stall bending flutter. The validity of the analysis for predicting this flutter mode is demonstrated by correlating the measured flutter boundaries of several high-speed fan stages with the predicted boundaries.

17. Key Words (Suggested by Author(s))	18. Distribution Statement
Actuator disk theory; Flutter; Supersonic speeds; Compressors	Unclassified - unlimited STAR Category 02

19. Security Classif. (of this report)	20. Security Classif. (of this page)	21. No. of Pages	22. Price*
Unclassified	Unclassified	57	A04

* For sale by the National Technical Information Service, Springfield, Virginia 22161

NASA-Langley, 1978

4 1 1U,A, 111378 S00903DS
DEPT OF THE AIR FORCE
AF WEAPONS LABORATORY
ATTN: TECHNICAL LIBRARY (SUL)
KIRTLAND AFB NM 87117